



HAL
open science

Upper crustal stratigraphy beneath the InSight lander on Mars and implications for its formation

V Ansan

► **To cite this version:**

V Ansan. Upper crustal stratigraphy beneath the InSight lander on Mars and implications for its formation. 2023. hal-03926771

HAL Id: hal-03926771

<https://hal.science/hal-03926771>

Preprint submitted on 6 Jan 2023

HAL is a multi-disciplinary open access archive for the deposit and dissemination of scientific research documents, whether they are published or not. The documents may come from teaching and research institutions in France or abroad, or from public or private research centers.

L'archive ouverte pluridisciplinaire **HAL**, est destinée au dépôt et à la diffusion de documents scientifiques de niveau recherche, publiés ou non, émanant des établissements d'enseignement et de recherche français ou étrangers, des laboratoires publics ou privés.

1 **Upper crustal stratigraphy beneath the InSight lander on Mars and**
2 **implications for its formation**

3 V. Ansan¹

4 ¹LPG-UMR CNRS 6112, University of Nantes, 2 rue de la houssinière, BP 92208, 44322
5 Nantes Cedex 3, France (veronique.ansan@univ-nantes.fr),

6 Version : may 2020

7 **Keywords:** Stratigraphy, Volcanism, Sedimentary filling, Martian regolith, Martian soil,
8 Elysium Planitia

9 **Key points:**

10 InSight landed on ~60 m thick, Early Amazonian, degraded volcanic flows overlapping >500m
11 thick, Late Hesperian layered volcanic material.

12 The upper part of 3m thick surficial unit is composed of poorly sorted, impact ejected magmatic
13 rocks interbedded in lens-shaped with aeolian deposit.~

14 The aeolian material consists of fine loose grains with high porosity at near-surface showing a
15 very weak cohesion at shallow depth.

16

17 **Abstract**

18 On November 2018, *InSight* landed at 4.502°N/135.623°E on the NW floor of ~27m-in-
19 diameter Homestead hollow in the western Elysium Planitia, composed of ~60m thick, Early
20 Amazonian degraded lava floods overlapping >500m thick Late Hesperian layered magmatic
21 material. Around the lander, the landscape appeared as a relatively flat rock-strewn cratered
22 plain with dunes far away. After the dust cleaning by retrorockets during the landing, the

23 interior of the hollow, bounded by a gently darker slope, showed a surface covered by a clastic
24 material, ranging from cobbles to sand, dominated by sand without aeolian bedforms. A
25 majority of rocks showing a dark, aphanitic texture with a probable volcanic composition are
26 interpreted to be impact ejected rocks due to their random spatial distribution, with a greater
27 number of rocks in the western side of hollow. Thanks to pits formed by retrorockets and HP³
28 mole penetration, the stratigraphy of hollow could be investigated, showing a meter-scale long,
29 ~10 cm thick lens-shaped interlayered deposits, with a pebble lens underneath the lander and a
30 sandy lens at HP³ location, composed of multi-layered very fine sand mixed locally to coarse
31 sand and granules poorly sorted, suggesting that the fine-grained material has been deposited
32 and homogenized by wind transport. Although this material shows a weak cohesion near HP³
33 after hammering tests, it would not be cemented by aqueous fluids. The ~3 m thick surficial
34 unit would be composed of superimposition of lens-shaped deposits mixing ejected rocks and
35 finer aeolian clasts, overlying the fractured Early Amazonian volcanic bedrock.

36

37 **1. Introduction**

38

39 The Interior Exploration using Seismic Investigations, Geodesy and Heat Transport
40 (InSight) is the first mission mainly dedicated to the understanding of the Martian internal
41 structure (Banerdt et al., 2013, 2020; Smrekar et al., 2019). Among its science tools are a
42 seismometer (Seismic Experiment for Interior Structure, SEIS) for detecting quakes (Lognonné
43 et al., 2019, 2020), a heat flow probe (Heat Flow and Physical Properties Package, HP³)
44 designed to take the planet's temperature (Spohn et al., 2018), including a radiometer (RAD)
45 instrument for measuring the surface brightness temperature (Spohn et al., 2018), a
46 magnetometer (InSight FluxGate, IFG), and sensors for gauging wind and air pressure (Gómez-
47 Elvira et al., 2012; Bandfield et al., 2019).

48 Determining the best landing site adequate for instruments safety and scientific success was
49 challenging. The pre-landing area had to be close enough to the equator to ensure power to the
50 lander solar panels, have a thick atmospheric column to deploy the parachute and slow down
51 the landing, be relatively flat, and consist of geological material that is both stable for the
52 seismometer and non-cohesive to facilitate the HP³ mole penetration (Golombek et al., 2017).
53 A 130 km x 27 km landing ellipse was selected in the western Elysium Planitia (Fig.1), ~500
54 km north of the Martian dichotomy and ~1,300 km southwest of Elysium Mons, in which the
55 mean elevation is around -2600 m without topographic relief except impact craters and wrinkle
56 ridges. At regional scale, the landing area would have been covered by at least 200 m thick
57 smooth volcanic material, locally showing lobate flow margins and probably consisting of
58 basaltic composition (Golombek et al., 2018; Pan et al., 2020). The subsurface would consist
59 of clastic material covering almost the entire region with an average thickness of 3 m and up to
60 18 m locally, derived from mapping of fresh, no rocky ejecta craters within the landing ellipse
61 (Golombek et al., 2017; Warner et al., 2017). Based on 100 meter-scale THEMIS data

62 (Christensen et al., 2004), a thin sandy layer (Presley and Christensen, 1997; Piqueux and
63 Christensen, 2011, Golombek et al., 2017) would cover the material of the Early Hesperian
64 transitional unit (eHt), comprised of layered volcanic and/or sedimentary materials (Tanaka et
65 al., 2014). So, all sub-surface property conditions were present for favoring both seismology
66 and heat flow acquisition (Golombek et al., 2017; 2018; Warner et al., 2017).

67 On November 26, 2018, the InSight lander (Banerdt et al., 2020) touched down at
68 $4.502^{\circ}\text{N}/135.623^{\circ}\text{E}$ (Parker et al., 2019; Golombek et al., 2020), ~25 km westward from
69 expected location (Fig. 1), in a probably highly degraded, ~1 m deep, ~27 m-in-diameter impact
70 crater in Elysium Planitia, called “Homestead hollow” (Golombek et al., 2020; Grant et al.,
71 2019, 2020; Warner et al., 2019, 2020). Although the hollow lacks a sharp rim, its boundary
72 shows a significant increase in rocks of cobble up to boulder size as compared to its relatively
73 smooth interior, composed of a majority of fine clastic material ranging from sandy to dusty
74 clasts mixed with few % of pebbles (Hauber et al., 2019; Grant et al., 2019; 2020; Weitz et al.,
75 2019, 2020). No aeolian bedform is identified within the hollow, although the region is subject
76 to seasonal winds of up to $25 \text{ m}\cdot\text{s}^{-1}$ (Spiga et al., 2018; Bandfield et al., 2020) at the lander deck
77 height of ~1.2 m above the ground, and dust devil tracks are identified near lander location
78 before and during the first 420 Martian days (Perrin et al., 2019; 2020; Rodriguez et al., 2019)
79 from High Resolution Imaging Science Experiment (HiRISE) images (McEwen et al., 2007).

80 The InSight landing site is characterized by an average surface magnetic field strength of
81 $2013 \pm 53 \text{ nT}$ with a direction south-east and upward (Johnson et al., 2020) which is ten times
82 stronger than predicted by satellite-based models (e.g. Connerney et al., 2015; Langlais et al.,
83 2017). Magnetization sources would be carried in older than 3.9 Gy basement crustal rocks
84 overlain by between 200 m and ~10 km of lava flows and modified ancient terrain (Johnson et
85 al., 2020). In addition, the upper crustal structure beneath InSight seems to be layered by ~10
86 km thick, highly altered or fractured volcanic material, inferred by three major marsquakes

87 that occurred during September, 2019 and the HP³ hammering activity (Giardini et al., 2020;
88 Lognonné et al., 2020).

89 The structure and the depth of upper subsurface layer remains poorly understood beneath
90 SEIS and HP³ instruments. As the HP³ mole started digging millimeter by millimeter into the
91 sub-surface, using the friction between clastic material and its sides to progress (Wippermann
92 et al., 2020), it began to tilt with a dip of ~15° to the southwest at a depth of 10 cm before its
93 sharp stopping at a depth of about 30 cm. While digging was helped using the robotic arm's
94 scoop to press on the side of the mole, the mole popped back out of the regolith on two
95 occasions, questioning about the structure of the sub-surface.

96 In this context, it is crucial to better understand the nature and the spatial structure of
97 subsurface beneath the lander and its nearby surroundings. Would it be close to a terrestrial
98 regolith, (i.e. a surficial geological formation resulting from the *in situ* fragmentation of rocks
99 by chemical and mechanical alteration without the elements having been transported), or rather
100 to a lunar regolith where the fragmentation of the rocks is essentially due to meteoritic impacts
101 (impact gardening)? What would be the contribution of sedimentary processes, such as wind-
102 driven sedimentation or diagenetic processes in its formation? What would be its detailed
103 structure (homogeneous or layered) and thickness? At which depth are the pristine lava flows?

104 In this study, we propose to revisit the local stratigraphy of the first hundreds meters of upper
105 crust, using a combination of orbital imagery and *in situ* imagery acquired by cameras on board
106 of the InSight lander, during the first 420 Martian days (sols) of the mission. From these
107 observations, we highlight the different lithology exposed in this area, their spatial distribution
108 and organization to propose a stratigraphic cross-section of the Homestead hollow and its
109 nearby surrounding. Finally, we discuss the nature, conditions of formation and timing of the
110 various geologic units, and the potential implications for the shallow crustal structure on
111 geophysical data acquired by SEIS and HP³.

112

113 **2. Data and methods**

114

115 In order to determine the stratigraphy beneath the InSight lander and its surroundings, we
116 use both orbital and ground datasets. Firstly, the multiscale orbital visible imagery gives us a
117 regional view of geological context. High Resolution Stereo Camera (HRSC) nadir images
118 (Neukum et al., 2004; Jaumann et al., 2007) and ConTeXt camera (CTX) images (Malin et al.,
119 2007) with an average resolution of 20 m.pixel^{-1} and 6 m.pixel^{-1} respectively, are used for the
120 identification of geological features like lava flows, lava fronts, and impact craters. Their
121 analysis is completed by HiRISE images (McEwen et al., 2007) for the fine details of geological
122 features with a spatial resolution of $0.25 \text{ m.pixel}^{-1}$. This dataset is reinforced by Thermal
123 Emission Imaging System (THEMIS) images (Christensen et al., 2004) to discriminate the
124 thermo-physical nature of surface material, at a resolution of 100 m.pixel^{-1} .

125 This analysis is performed in association with altimetry data at different scales, including
126 topography acquired by Mars Orbiter Laser Altimeter (MOLA) (Smith et al., 1999) at ~ 463
127 m.pixel^{-1} , and Digital Elevation Models (DEM) made from CTX and HiRISE stereo pairs
128 processed by Ferguson et al. (2017), at spatial resolution of 20 m.pixel^{-1} and 1 m.pixel^{-1}
129 respectively, with a vertical accuracy close to 0.13 m and 4.0 m respectively. All orbital data
130 are implemented in GIS, using Equirectangular projection equally sampled in planetographic
131 latitude, with elevations referenced to the MOLA-defined geoid (Smith et al, 2001).

132 Secondly, the ground color imagery is performed both by the Instrument Context Camera
133 (ICC) placed on the lander, showing the wide-angle view in front of lander with an angular field
134 of view of $2.1 \text{ mrad.pixel}^{-1}$ at the center of the image (Maki et al., 2018), leading to a spatial
135 resolution of $\sim 6 \text{ mm.pixel}^{-1}$ at a range of 3 m from the lander, and the Instrument Deployment
136 Camera (IDC), mounted to the lander robotic arm acquiring images of the lander and

137 surrounding terrain with an angular resolution of $0.82 \text{ mrad}\cdot\text{pixel}^{-1}$ at the center of the image,
138 corresponding to a spatial resolution of $\sim 0.5 \text{ mm}\cdot\text{pixel}^{-1}$ at a range of 0.65 m from the IDC
139 (Maki et al., 2018). The topography of the instrument deployment workspace, a $4 \text{ m}\times 6 \text{ m}$ area
140 located in front of the lander, was performed from Stereo IDC image pairs, acquired by moving
141 the arm between images (Trobi-Ollennu et al., 2018), with a horizontal post spacing ranging
142 from 0.5 to $2 \text{ mm}\cdot\text{pixel}^{-1}$ (Maki et al., 2018; Abarca et al., 2019). These ground data were
143 mosaicked and projected in Cartesian coordinates in Site or lander frame (see Abarca et al.,
144 2019 for details).

145 The stratigraphy of Homestead hollow was made, using both the main concepts of
146 lithostratigraphy (Stenonis, 1669) based on the law of superposition (relative age), the principle
147 of original horizontality and the principle of lateral continuity, and planetary chronostratigraphy
148 based on impact crater size-frequency distribution derived from the Moon (e.g. Hartmann,
149 1970; Neukum et al., 1975, Neukum et al., 2001) and extrapolated to Mars (e.g. Ivanov 2001;
150 Hartmann 2005). So, crater-counting methods were used to estimate the absolute ages of
151 surface units. Crater counts were performed on orbital THEMIS, HRSC and CTX data. A
152 sinusoidal projection was used for the crater counts. Buried craters (with no or partial rims
153 exposed, often named ghost craters) were not included in the crater counts of units nor were
154 dense fields of secondary craters. Crater statistics and crater model ages were analyzed with
155 Craterstats2 software (Michael and Neukum, 2010; Michael et al., 2012; Michael, 2013), using
156 the production function of Ivanov (2001) and the chronology Hartmann and Neukum (2001).
157 Combining all cartographic information (spatial organization and age) with landforms and
158 geologic features (e.g. bedforms, layers, rock/clast textures...) from orbital and in situ data,
159 geologic cross-sections and logs were performed at the InSight landing site.

160

161

3. Regional Stratigraphy from orbital data

The previous geological studies showed that the region is covered by at least 200 m thick smooth volcanic material, probably consisting of basaltic composition (Ansan et al., 2015; Golombek et al., 2018; Pan et al., 2020), using a wide variety of imaging during the landing site selection process. These data indicated that this volcanic material had to be overlapped by a dominantly sandy material with low rock abundance, interpreted as ~3–18 m thick, impact fragmented, unconsolidated regolith overlying coarse breccia that grades into jointed basalt (Golombek et al., 2017; 2018, 2020; Warner et al., 2017). A relatively thin dust layer (dust index of 0.94, Ruff and Christensen, 2002) covering the area was regularly swept by seasonal winds (Spiga et al., 2018) raising dust devils (Reiss et Lorenz, 2016; Reiss et al., 2016) whose traces scar the surface at metric scale of High Resolution Imaging Science Experiment (HiRISE) images (McEwen et al., 2007).

Geological units

Here we revisit the geological units identified in the vicinity of the landing site (~50 km), showing that the region is essentially composed of layered volcanic material covered by clastic material whose source is both impact ejected rocks and eolian sediments.

While the western Elysium Planitia is relatively flat, the InSight lander touched down on the eastern side of ~NNW-SSE trending, 25 km wide, 80 km long ridge raising ~65 m above the surrounding plain (Fig. 1b and d), based on MOLA topography at ~500 m.pixel⁻¹. The topographic slope of the ridge side is lesser than 0.4°, which is in good agreement with the pre-landing recommendation (Golombek et al., 2017). This broad ridge could be either the result of volcanic edifice or tectonic structures. The first assumption seems to be rule out because we

187 observe no obvious primary volcanic landforms at its summit, such as volcanic vents, or
188 fractures, at THEMIS and HRSC scale.

189 The broad ridge is framed by two parallel, 10 km wide, 10s km long, <50 m high, sinuous
190 wrinkle ridges, recognizable by their asymmetrical morphology and crenulation at their crest
191 (e.g. Maxwell et al, 1975; Chicarro et al., 1985; Watters, 1988; Schultz, 2000; Golombek et al.,
192 2001). Wrinkle ridges are usually interpreted as compressive tectonic structures (i.e. folds
193 and/or fault-related folds (e.g. Watters, 1988, Suppe and Narr, 1989; Allemand and Thomas,
194 1992; Mangold et al., 1998; Mueller and Golombek, 2004; Golombek and Phillips, 2009),
195 created during the cooling and contraction of the magmatic plume below the volcanic plain, or
196 the whole planet. The broad elongated topographic ridge is then interpreted as an “arch”, first
197 characterized in lunar mare (e.g., Strom, 1972; Bryan, 1973; Maxwell et al., 1975), consisting
198 of a broad, low-relief tectonic pop-up structure. Although the formation of wrinkle ridges
199 requires the presence of any layered upper crust, regardless of the nature of the layering, they
200 are commonly thought, based on lunar analogy, to form in volcanic terrains composed of stacks
201 of lava flows.

202 At CTX resolution, this interpretation is supported by the presence of relatively flat
203 landforms that are lobate in plan view, characteristic of volcanic lava flow fronts (Golombek et
204 al., 2018). A few kilometers east of the landing site, at least three superimposed lava flows are
205 identified (Fig. 1c), with an apparent eastward flow direction. Based on CTX DEM, the typical
206 thickness at the front of individual flows is ranging from 5 m to 40 m (Fig. 1h), assuming a
207 local horizontal dip, which is quite common on Elysium Planitia (e.g. Vaucher et al, 2009). Due
208 to their morphology and their extent, these lava flows were likely composed of relatively low
209 viscosity material during their emplacement. However, it is quite difficult to find local vents
210 or fractures from which lava flows originated.

211 Around the landing site, the relatively flat and shallowly sloping volcanic surface at CTX
212 scale (Fig. 1c) appears rough and heavily cratered with craters smaller than 200 m in diameter
213 at HiRISE scale (Fig. 1g), without reaching a saturation density (i.e. old impact craters are not
214 packed tightly enough to be destroyed by the creation of new craters (Chapman and McKinnon,
215 1986; Hartmann, 1995)). The large population of small craters was previously interpreted
216 (Golombek et al., 2017) as a dominant impact-induced regolith (i.e. a layer of unconsolidated
217 solid clastic material covering the bedrock of a planet, due to impact gardening). In this
218 scenario, when meteorites impact the Martian surface, the surface is fragmented, the sub-
219 surface material is partly excavated forming a cavity (crater), and ejected into atmosphere
220 before re-impacting around the crater forming an ejecta blanket (Melosh, 1989). When the
221 impact process is replicated thousands of times at the same place, a regolith layer forms with a
222 clast distribution decreasing in size to the top of the layer (Charalambous, 2015), as observed
223 on the Moon.

224 At HiRISE scale (Fig. 2b,c and d), the volcanic surface is cratered by 1-200 m-in-diameter
225 impact craters, relatively spaced with rocky ejecta for those greater than 30 m in size (Warner
226 et al., 2017). Although many small impact craters are surrounded by an ejecta blanket, many
227 of them show a significant degree of degradation. At HiRISE scale (Fig. 2), numerous craters
228 with a diameter ≥ 30 m do not show a classic radiating boulder-rich ejecta but a remnant
229 discontinuous ejecta blanket, testifying to significant degradation by aeolian processes in
230 privileged directions, leading to the preservation of a star pattern in the ejecta (Fig. 2d, impact
231 crater in box labelled c and Fig. 4g). This suggests that the area is subjected to winds carrying
232 sandy materials that cause ejecta abrasion.

233 Sand accumulated near the crater rims forms either leeward wind streaks (e.g. three bright
234 wind streaks (WS) radiating from fresh impact craters, as in the lower right corner of Fig. 1c),
235 or bright crescent-shaped, 10s m long, 10 m wide, ~1 m high dunes on the windward side (Fig.

236 2). These dunes appear immobile if we compare their location between May 2014 and
237 December 2018, which seems to be in agreement with the light tone of the dunes surface (Baker
238 et al., 2019). Indeed, most mobile dunes display a low albedo, due to their mineralogical
239 composition. Dark dunes are composed of basaltic igneous minerals such as olivine, pyroxene
240 and plagioclase, as detected by orbiter-based thermal infrared and visible/shortwave-infrared
241 (VSWIR) spectroscopic measurements (e.g. Christensen et al., 2000; Bibring et al., 2005;
242 Poulet et al., 2009; Rogers & Bandfield, 2009; Tirsch et al., 2011) and rover X-ray diffraction
243 (XRD)/X-ray fluorescence measurements (e.g. Achilles et al., 2017; Rampe et al., 2018). Dark
244 dunes become lighter-toned due to a reddish dust mantling and internal grain size and
245 organization (Blake et al., 2013), although some dunes, such as small ripple dunes and
246 transverse aeolian dunes, are suspected to be light-toned and formed by dust clumps (e.g Balme
247 et al., 2008; Zimbelman, 2010; Geissler, 2014). In addition, ripple and dune fields are locally
248 observed inside relatively larger impact craters (Fig. 2c).

249 For the small craters and intercrater areas near the landing site, the infilling material is
250 characterized by a relatively smooth, medium grey-toned surface (Fig. 2). This surface appears
251 scoured by 100s of meter long, <10 m wide, dark, rectilinear features, although these features
252 continue in the surrounding rougher areas with a more subdued tone (Fig. 2a, b, d). In HiRISE
253 image acquired in May 2014 (Fig. 2 a, b) and in December 2018 (Fig. 2d), numerous rectilinear
254 dark albedo features are visible with a dominant trend of NW-SE. They are the result of dust
255 devils (e.g. Balme & Greeley, 2006; Cantor et al., 2006; Reiss et al., 2016), raising the dust
256 accumulated from regional and global Martian storms (e.g. McKim, 1996; Cantor, 2007,
257 Guzewich et al., 2019) During the first 420 sols of the InSight mission, many new linear dark
258 tracks caused by dust devils have been detected near the InSight landing site in orbital images,
259 showing seasonal variations of their frequency and directions (Perrin et al., 2020).

260 In summary, the InSight landing area is composed of two main units: a volcanic unit
261 consisting of stacked volcanic flows cratered by small impact craters, and a surficial unit
262 consisting of aeolian deposits (sand and dust) mixed with rocky ejecta formed by impact
263 gardening, as distinct from a *sensu stricto* lunar regolith.

264

265 *Age of geological units*

266

267 As we observed previously, the volcanic surface is characterized both by a small population
268 of >1km-wide fresh impact craters (i.e. with ejecta blanket) in an area between 4°N and 5.6°N
269 and 135° and 137°E (Fig. 1b, f, Fig. 3). In order to determine the surface retention age, we
270 selected all well-preserved impact craters with ejecta blanket (fresh impact craters) post-dating
271 the surface. On the area (S_{HRSC}) covering 10,437.099 km² (Fig. 3), 14 impact craters have been
272 identified with a diameter ranging from 1.08 km to 8.83 km, based on THEMIS and HRSC
273 images. Within this widespread area, a smaller area has been selected from CTX images
274 centered on the InSight landing site (Fig. 3, S_{CTX} , 1,642.369 km²) in which 11,496 impact craters
275 are identified with a diameter ranging from 20 m to 1.50 km. The crater count has not been
276 performed for <150 m-wide craters, due to the high degree of surface degradation.

277 Based on this dataset, crater counts were carried out on the volcanic unit to estimate its
278 individual absolute model age of formation (Fig. 3). Based on THEMIS and HRSC images,
279 the regional volcanic surface has a crater retention age of 3.6 + 0.1/-0.2 Ga (i.e. the boundary
280 between Early Hesperian and Late Hesperian in Neukum-Ivanov's chronology system;
281 Neukum and Ivanov, 2001), following well the isochrons of Ivanov (2001) for impact craters
282 greater than 2 km in diameter (black line in Fig. 3).

283 Using the smaller crater population enables the actual surface age of the volcanic surface,
284 after a degradation event, to be characterized. Indeed, a kink in the size-frequency plot occurs
285 for crater diameters ranging between 1.5 km and 2 km. Resurfacing process (red curve in Fig.

286 3) then overprinted the entire studied area until $2.6 + 0.5/-0.7$ Ga (i.e. Early Amazonian in the
287 chronology system of Neukum and Ivanov (2001)), following well the isochron of Ivanov
288 (2001) for impact craters ranging from 200 m to 2.0 km-in-diameter.

289 Interestingly, this secondary retention age is of the same order as that of the volcanic flows
290 estimated from a cumulative crater size-frequency distribution at CTX scale (i.e. 2.6 ± 0.1 Ga,
291 green curve in Fig. 3, for impact craters ranging from 150 m to 700-in-diameter), showing that
292 resurfacing probably occurred as a volcanic episode during the Early Amazonian. This last
293 widespread volcanic event buried most impact craters smaller than 2 km-in-diameter.

294 Since this period of time, the area has been subjected to a continuous degradation process
295 affecting <200 m-in-diameter impact craters because the crater size distribution below this
296 diameter crosscuts all isochrons younger than 2.6 Ga. With respect to geological processes, the
297 degradation is most likely due to aeolian erosion and deposition (dust and sand). At CTX scale,
298 there is no difference in retention age between the surface of the volcanic ridge (western area)
299 and the surface of the eastern plain, which prevents the determination of the ages of each lava
300 flow identified on the eastern side of ridge (Fig. 1c).

301

302 *Thickness of geological units*

303

304 In the case of western Elysium Planitia where InSight landed, the difficulty for determining
305 the thickness of geological units is the lack of exposed sections of the stratigraphy, such as
306 topographic scarps. However, impact craters are windows into the subsurface that enable the
307 extraction of geological information crucial to the understanding of geological structure, with
308 a few precautions. Using relative chronology relationships (craters crosscutting or overlain by
309 a formation, Fig. 1e, d) and crater morphometry relationships (Table 1), it is possible to estimate
310 the thickness of volcanic material at InSight landing site, discriminating the Early Amazonian

311 volcanic surface due to regional resurfacing from the probable Hesperian volcanic bedrock.
312 Then, the thickness of sedimentary units will be estimated by the same method.

313 Assuming that the Early Amazonian volcanic material within the ridge belongs to volcanic
314 material covering the regional area (i.e. area viewed in Fig. 1b and f), its minimum thickness
315 could be estimated from the buried impact craters. Indeed, the minimum thickness of volcanic
316 flow may be estimated from the rim heights of several buried craters emerging above the lava
317 surface (Fig. 1e, crater #1). These rim heights had to be reached before the lava could fill the
318 impact crater (Fig. 1e, craters #2 and 3). The crater rims heights (h) above the surrounding level
319 are then estimated, using the average relationships between rim heights and diameters (D) for
320 fresh impact craters on Mars (Table 1), based on the measurement of 6000 impact craters in
321 MOLA data (Garvin et al., 2003).

322 We identified 6 partly to completely buried large impact craters in the Early Amazonian
323 volcanic material of the surrounding of landing site (Fig. 1f) and we measured their rim-to-rim
324 diameter from HRSC images (Table 2). Although the population of filled craters is small
325 around the landing site, three buried craters frame the area to the north and south, providing an
326 estimate of minimum Amazonian lava thickness (T) between 56 and 186 m (Table 2). We
327 could compare it with that expected for partly filled craters using the same dataset (i.e. MOLA
328 altimetry).

329 We calculated the remnant relief of crater rim (h_r) from the difference of the maximum
330 MOLA elevation of rim (h_{r_max}) and the mean plain elevation (h_{plain}) measured at a distance
331 of one crater diameter from the crater rim. Then we calculated the minimum Amazonian lava
332 thickness (T) as the difference between the expected rim height as calculated with Garvin's
333 morphometry relationship (h) and the measured remnant (or current) rim height (h_r , Table 2).
334 Except the crater c6, the minimum lava thickness is of the same order (~60 m) as that calculated

335 from the crater rim of buried craters. Due to the lack of completely filled craters very close to
336 the landing site, it can be estimated that the minimum lava thickness is at least 60 m.

337 In addition, this estimated lava thickness is consistent with that deduced from the maximum
338 size of degraded craters due to resurfacing process by volcanic flows occurred at 2.6 Ga (red
339 curve in Fig. 3). Indeed, a kink appeared in the cumulative size-frequency distribution of impact
340 craters for craters smaller than 2 km-in-diameter that have an average rim height of ~60 m,
341 calculated from Garvin's crater morphometry for simple bowl-shaped impact craters (i.e. $T = h =$
342 $=49.5$ m, Table 1) and from Watters et al.'s relationship for small impact craters (i.e. $T = h =$
343 71.6 m, Table 1). So, the average estimation of lava thickness for the last volcanic event (i.e.
344 at ~2.6 Ga Early Amazonian) is ~60 m.

345 Although the partly buried impact craters show inner degradation such as sedimentary
346 filling, rim slumps and landslides, they give us some information about the nature and the
347 thickness of the Hesperian bedrock (Fig. 4) on which the Early Amazonian lava was deposited.
348 For example, the c#6 crater shows a 900 m deep central depression with relatively well
349 preserved inner rim (Fig. 4b) and flat floor. Below the crater rim, ~500 m thick dark layered
350 material is identified in the crater side (L in Fig. 4d). It is also observed in the inner side of an
351 impact crater of the same size, located 50 km north of c#6, post-dating Early Amazonian lava,
352 with 400m of stratified dark layered material under its rim (Fig. 4c, e). For impact craters larger
353 than 9 km, no data are available to observe the bedrock due to degradation or modification of
354 the inner crater edges. This suggests that the bedrock would consist of a series of volcanic lava
355 flows at least 500 m thick. Unfortunately, the lithology cannot be determined mineralogically
356 by near-infrared data due to the presence of dust.

357 In addition, all craters with an ejecta blanket post-date the Early Amazonian volcanic
358 surface. Depending on their diameter, they can penetrate the Early Amazonian volcanic material
359 and the underlying Hesperian volcanic bedrock, with no distinction between the two, e.g. crater

360 #4 in Fig. 1d). Indeed, impact craters greater than 300 m and smaller than around 1 km, post-
361 dating the Early Amazonian lava flows, have dark rocky ejecta blankets both in daytime
362 THEMIS images (Fig. 1c) and in HiRISE images (Fig. 2c, 4g), interpreted as rocky volcanic
363 material (Golombek et al., 2017; Warner et al., 2017). Using the crater morphometric
364 relationships for relatively pristine impact craters (Table 2), the depth of these craters is thus
365 ranging from 81 m using Sweeney et al.'s morphometry relationship (Table 1) to 210 m using
366 Garvin et al.'s morphometry relationship (Table 1). Therefore, these craters have impacted
367 volcanic material with a thickness exceeding 200 m, which is very consistent with the thickness
368 of volcanic material of undifferentiated age as previously estimated from large impact craters
369 (Golombek et al., 2017; 2018).

370 Since the Early Amazonian, the area is subjected both to aeolian erosion and sedimentation
371 (this study, Warner et al., 2017 and 2020; Sweeney et. al, 2018). Many impact craters \leq 200
372 m-in-diameter show degraded impact rims with boulders (Warner et al., 2017) and scours from
373 aeolian abrasion. Based on this observation and rim crater morphometry relationships (Table
374 1, Watters et al, 2015 and Sweeney et al. 2018), the surface could have lost ~6m in thickness
375 by aeolian erosion.

376 The thickness of the surficial unit, consisting of aeolian deposits (sand and dust) mixed with
377 rocky ejecta, is estimated from very small impact craters observed on HiRISE images, using
378 crater morphometry relationships (Table 1). The smaller fresh impact crater whose excavation
379 depth can be calculated by Sweeney et al. (2018) is 10m, giving a excavation depth of 0.8 m,
380 comparable to that measured from HiRiSE DEM (Fig. 4f, g). All impact craters smaller than
381 30 m, observed within a radius of 1 km around the landing site, show no boulders within their
382 partly preserved ejecta (Fig. 2 c, d), which suggests that the impacted material is composed
383 essentially of a loosely consolidated, fine-grained material with particle sizes smaller than
384 boulders (Golombek et al., 2017; Warner et al., 2017;). Using crater morphometry relationship

385 (Table 1, Sweeney et al., 2018), the thickness of fine-grained material without boulders is 2.5
386 m. This thickness is consistent with the previously estimated thickness of regional surficial fine-
387 grained “regolith” (i.e. 2-5 m (Warner et al., 2017) and i.e. ~3 m (Warner et al., 2020)).

388 The surface of Homestead hollow is covered by dust mantling whose thickness was
389 evaluated only from the analysis of TES and THEMIS thermal inertia data, showing an average
390 thermal inertia of around $200 \text{ Jm}^{-2} \text{ K}^{-1} \text{ s}^{-1/2}$ that is consistent with surface grain sizes of fine
391 sand and a <1-2 mm thin dust layer (Golombek et al., 2017, 2018).

392

393 *Stratigraphy from orbital data*

394

395 Based on the geomorphological, geological and chronological analyses of orbital data
396 covering the landing site, we propose the following stratigraphy (Fig. 5): The area was covered
397 by very thick (> 500m) volcanic material dated at 3.6 Ga corresponding to the boundary of
398 Early/Late Hesperian.

399 A regional resurfacing event occurred at 2.6 Ga during the Early Amazonian, interpreted to
400 be the last widespread volcanic flows covering the highly cratered Early/Late Hesperian
401 volcanic surface, with a thickness of ~60 m, covering most craters below ~2km-in-diameter.
402 Although this volcanic material was then deformed by wrinkle ridges, and degraded by small
403 impact craters, its layered structure and its volcanic landforms (lobate fronts) are relatively well
404 preserved.

405 Above this volcanic material, a granular, unconsolidated unit covers the surface with a
406 variation in grain size and thickness. This surficial unit is composed both of clasts coarser than
407 boulders ejected from ≤ 200 m-in-diameter impact craters and smaller clasts of eolian origin.
408 This surficial unit shows notable thickness variations (i.e. 3-17m at regional scale (Warner et
409 al., 2017), but the thickness of the upper part of surficial unit containing only clasts smaller than

410 boulders seems to be limited to 2.2-3 m in Homestead hollow, based on the surrounding no
411 rocky ejecta crater ≤ 30 m-in-diameter.

412

413 **4. Stratigraphy from *in situ* data**

414

415 On December 18, 2018, InSight landed at 4.502°N, 135.623°E at an elevation of -2613.43
416 m, on a relatively flat area slightly inclined 1.3° to the SE (Fig. 1g, 2), in the northwestern part
417 of a ~27 m wide near circular depression, interpreted to be a degraded impact crater (Warner et
418 al., 2020), informally named Homestead hollow. The depth of depression is estimated to be \leq
419 0.8 m from HiRISE DEM (Fig. 6c and d). At HiRISE image scale, the surface texture of the
420 depression is very smooth with very few boulders and small impact craters lesser than 3 m in
421 diameter (Fig. 2e, f), suggesting that the sub-surface is composed of fine-grained material
422 smaller than boulders.

423 During the landing, the dust layer was lifted into the atmosphere by retro-propulsive rockets
424 enabling to slow the lander's descent and perform a safe soft landing, which led to cleaning the
425 surface and redistributing primarily fine-grained materials. The surface alteration is easily
426 identified as "halo" of albedo and/or color variations in HiRISE images (Fig. 2d, f, g). These
427 images reveal a relative brighter inner halo extending up to 8-11 m from the lander that has an
428 18% lower relative albedo compared to unaltered background, surrounded by a relative darker
429 outer halo extending from the edge of the high reflectance halo out to 15-21 m from the lander
430 that has up to a 35% lower relative albedo compared to the unaltered surface (Williams et al.,
431 2019).

432 The relative darker outer halo also extends more weakly much farther to the southeast along
433 the prevailing wind direction (Forget et al., 1999; Spiga et al., 2018; Bandfield et al., 2020).
434 Additionally, a discontinuous pattern of low-reflectance rays (dark-blueish tones in false-color

435 (Infrared, Red and Blue) IRB HiRISE image, Fig. 2g) extends primarily towards the north up
436 to 5 m from the lander. The relative darkening of the surface is thus consistent with the expected
437 removal of a thin layer (microns) of dust during landing (Golombek et al., 2020), similar to
438 previous Mars landing sites (e.g. Johnson et al., 2014; Daubar et al., 2016) and analogous to the
439 formation of typical dust devil tracks (Reiss and Lorenz, 2016). Although much brighter than
440 the outer halo, the relative brighter inner halo is still darker than the unaltered surface and it
441 was likely covered by a veneer of dust that is now removed.

442 The presence of dust at the time of landing is also demonstrated by the first images acquired
443 by the two cameras on the lander board, in particular by the wide field of view (ICC) whose
444 cover did not sufficiently protect the optics (Fig. 7). A few days after landing, the dust particles
445 fell off the optics and the images were clear (Fig. 7), due to a cleaning by the wind activity in
446 the area as measured by wind sensors (e.g. Bandfield et al., 2020, Charalambous et al., 2020).

447

448 *Landing site viewed from the ground*

449

450 In the following sections, we describe the landforms and the surface materials observed in
451 front of and beneath the lander, based on IDC images and DEMs. InSight lander touched down
452 the surface with a low tilt of 3.975° towards the SE (133.408 degrees clockwise from the North)
453 (Fig. 6), interfering with the data acquisition on the ground, near the lander, in particular in the
454 NW part where the radiometer (RAD) instrument acquires the surface temperature. As
455 expected, the solar lander panels were deployed and oriented ~E-W (Fig. 2f, g), enabling the
456 ICC camera looking southward (Fig. 7). In this south view of Homestead hollow, the landscape
457 appears relatively flat, with a smooth surface on which no sedimentary bedforms (ripples,
458 dunes) are present, except for rocks that are typically smaller than cobbles and scattered
459 randomly (Fig. 7).

460 InSight's Instrument Deployment Camera (IDC) located on the lander's robotic arm
461 acquired red/green/blue (RGB) color images from a height of ~1.5 m above the surface,
462 including a panorama of mid- and far-field terrain around the lander on sol 14. In the mid-field
463 panoramic view around the lander looking eastward (Fig. 6a), the dark halo and the brighter
464 central part of Homestead hollow are still recognizable. The landscape is relatively flat with
465 approximately a dozen bright-reddish 1–10m wide circular shallow depressions (c# in Fig. 6a)
466 within 20 m of the lander, interpreted as impact-generated depressions filled with granular
467 material (Golombek et al., 2020). No outcrops are present within the very shallow (~ 0.8 m
468 deep in IDC DEM, Fig. 6b) Homestead hollow, delineated by a darker, ~0.4 m tall, gentle north-
469 facing rise of 3° in the SSE looking (Fig. 6a,b,e), beyond which many boulders and rocks strew
470 the surface (Fig. 8).

471 Within the Homestead hollow, the surface is relatively smoother and brighter to the far east
472 of the lander than in its western and southwestern parts where rocks, ranging from cobbles to
473 pebbles, are randomly distributed and spaced apart (Fig. 6a, 8), as discussed in details by Grant
474 et al., 2020. The rocks partially cleaned by the rocket blast show different shades, shapes and
475 textures (Fig. 8): There are either dark-toned rocks probably composed of volcanic material
476 such as basalt, or light-toned rocks, often smaller than the former, possibly composed either of
477 brighter volcanic material such as andesite or cohesive sedimentary material excavated by
478 impact from a near-surface sedimentary layer. However, these lithological proposals should
479 be taken with caution since no microscopic and mineralogical analysis instruments are included
480 in the InSight instrument package. Most of these rocks show relatively angular equant shapes
481 and pyramidal shapes typical of wind erosion (i.e. wind-faceted rocks w/o ventifacts, Fig. 8c,
482 e). Some of them are cross-cut by sharp fractures possibly due to thermal weathering (thermos-
483 clasty) and/or shock from ejecta fall. Although the rock texture is quite difficult to define at
484 this distance away from lander, few rocks show an assembly of cohesive centimeter-sized

485 components, suggesting a brecciated texture (Fig. 8f). Note that many rocks has a redder area
486 on the ground radially outward from the lander, suggesting that a thin layer of material may
487 have remained in place during the blowing produced by the lander retrorockets.

488

489 *Landforms and geology in front of lander*

490

491 A large number of color images, including stereo coverage, were acquired by the arm-
492 mounted IDC camera, imaging the $\sim 6 \text{ m} \times \sim 4 \text{ m}$ workspace tilted $\sim 4^\circ$ to the southeast in front
493 of the lander (Fig. 6b, 9), to select the locations to place the geophysical instruments. The
494 smooth workspace surface is covered by a majority of sand-sized grains with scattered $> \text{cm}$
495 scale clasts (e.g. Golombek et al., 2020; Grant et al., 2019, 2020; Hauber et al., 2019; Weitz et
496 al., 2019, 2020), ranging from pebbles to very few cobbles in Wentworth's granulometry
497 classification (Wentworth, 1933). Large clasts show two types of materials: one is dark-toned,
498 grey aphanitic at the IDC resolution of $\sim 1 \text{ mm}$ at this distance (Fig. 9a, b, c and k), probably
499 corresponding to a basaltic composition, and the other one is light-toned with no visible texture
500 and unknown composition (Fig. 9i, j) possibly a cohesive mix of sand and dust. The dark clasts
501 show sub-equant shape with sub-angular edges while the light clasts are close to thin, platy
502 shape with angular to sub-angular edges (Fig. 9). Some of dark clasts seem to be composed of
503 different aggregated elements, suggesting that they may form a brecciated material (Fig. 9a,d,
504 f).

505 In addition, the clasts are usually covered by very thin reddish material whose nature remains
506 unclear (layer or coating), suggesting they have been on the surface for a long time despite the
507 cleaning of the retrorockets. Numerous clasts are partially buried (Fig. 9d, h, j), showing that
508 sedimentary processes are or were active after their deposition. Finally, the retrorockets not
509 only cleaned the surface of the dust, but also dislodged small pebbles and even threw them a

510 few tens of centimeters from their original position (Fig. 9e, h, i) (Golombek et al., 2020), either
511 by dragging or skipping and rolling leaving their footprints in the ground (white arrows),
512 especially near the western lander foot as observed on ICC images (Fig. 7).

513 In a more restricted area of the workspace very close to the lander (Fig. 10), a mosaic of IDC
514 ortho-rectified images with a very high resolution (scale: 1 mm.pixel⁻¹) enables to determine the
515 size and the shape of 8,252 clasts. Their edges are digitized as polygonal outlines in GIS
516 package, and the length and the width of each clast are measured in metric coordinates. The
517 majority of measured clasts belongs to very small pebble class, ranging from 2mm to 50 mm
518 with a mean size of ~6 mm (Fig. 10b). The shape of these clasts in 2D is close to be circular
519 with almost the same length in two orthogonal trendings (i.e. equant to sub-equant, Fig. 10c)
520 (e.g. Hauber et al., 2019; Weitz et al., 2019, 2020; Golombek et al., 2020).

521 While the surface between the rocks appeared smooth just a few meters from the lander, the
522 ground surface is striated and scoured, with multi-millimeter relief ridges and troughs that
523 extend radially away from the lander (Fig. 11). Some granules and small pebbles have tails
524 extending away from the lander, suggesting that material behind small clasts has been preserved
525 from the erosive rocket blast. The removed clastic material is thus smaller than millimeter (i.e.
526 sand at least), but its grain size cannot be precisely determined due to the resolution limits of
527 the IDC camera (i.e. >0.5 mm.pixel⁻¹).

528 In addition, this sandy material is not cohesive, enabling the displacement of clasts by rocket
529 blast. This is also supported by (Fig. 12): 1) the displacement of coarse sand/granule grains
530 (2.5±0.7 mm) over a distance of ~2 cm, during an aeolian gust occurred sol 283 (Fig. 12f,g); 2)
531 the “splash” features on the surface of HP³ foot that are oriented parallel to the measured wind
532 direction during this event, suggesting that sandy particles impinge on the surface after a
533 transport of saltation (Fig. 12h,i); 3) the mass-wasting of scour sides previously formed by retro-
534 rockets, leading to partial removal and new arrangement of fine-grained material transported

535 by creeping towards NE trending as marked by the reshaping of scours, and imprinted by faint
536 striation into the ground (Fig. 12d,e). See more detailed information in Charalambous et al.,
537 2020, Charalambous et al., submitted in GRL and Baker et al. submitted in JGR.

538 Despite the lack of aeolian bedforms such as ripples, the surface of Homestead hollow is
539 subjected to wind activity, reshaping the surface roughness sporadically. The dust fallen few
540 hours/days after the landing and during the regional dust storm (sol40-sol52) (e.g. Viudez-
541 Moreiras et al., 2020) was removed also on the small pebbles (Fig. 12) and on solar panels
542 (Lorenz, 2020) during different gusts monitored at landing site (Bandfield et al., 2020; Spiga et
543 al., 2020). However, no image has captured a dust devil to date.

544

545 *Sub-surface at location of HP³ mole penetration*

546

547 During sol 76 (February, 12, 2019), the HP³ instrument was placed on the ground ~1.5 m
548 from the lander in a SSE direction. Few days later, the hammering test started, but the 2.7 cm
549 diameter mole only partially penetrated into the sub-surface up to ~30 cm deep with a tilt of
550 ~15°. Due to the stalling of the mole penetration, it was decided to lift the HP³ cover, in order
551 to visualize the hole made by the mole.

552 A steep-sided open pit ~5 cm wide and ~5 cm deep appeared between circular imprints of
553 the HP³ feet (Fig. 13a, 14). These imprints with a depth of a few mm, showed a very fine-
554 grained sandy layer with sparse coarse sand grains. This layer was sampled, lifted up to 50 cm
555 above the ground and redeposited on the ground by the east rear HP³ foot, without losing its
556 cohesion, suggesting that this fine sand is weakly indurated or that the sand particles are very
557 fine in order to be held together by electrostatic forces as flour would behave (Fig. 13e-g).

558 In addition, the open pit did not show any significant piles of excavated granular material
559 around the hole, which suggests the underlying material has a low density and/or high porosity

560 because it was compressed by the mole hammering. The steep pit walls showed also a layered
561 material composed of relatively dark fine sand with sparse coarse sand grains in the uppermost
562 ~2 cm as in the imprints of HP³ feet. In order to support the mole penetration, several pushing
563 scoop tests have been performed close to the mole (Fig. 13c, d). The first imprint of the scoop
564 at the surface (Fig. 13c) was around 0.5 mm deep with a relatively flat surface without cracks.
565 After several scoop pushing tests, the top surface remained relatively flat and horizontal, but
566 mass-wasting and collapsing with relatively flat slope occurred in the upper granular material
567 in the west side of the hole, showing the very fine layering controlled by the grain size (Fig.
568 13d). The topographic profiles across the scoop indentation shows the upper layer has been
569 compacted vertically by ~1 cm (Fig. 14), indicating that the material is unconsolidated granular
570 and its porosity would be quite high.

571 This fine-grained layer overlapped a layered material composed of granules/small pebbles
572 and sand, interstratified with very fine sand or dust. The laminae containing granules/small
573 pebbles seem to have a higher degree of cohesion than finer ones, because the coarse clasts
574 remained in overhangs (Fig. 13a, b). However, when a last pushing test was made, these
575 granules, small pebbles and clumps collapsed and partially filled the hole (Fig. 14b, c),
576 suggesting that the cohesion is quite low in this coarser material. Note that a few dark-toned,
577 rounded, ~5 mm in diameter pebbles seem to be aggregated together without any visible cement
578 (Fig. 13b). In addition, the clumps lining the bottom of the hole appear to consist of an
579 aggregate of coarse sand/granule grains in a finer-grained matrix, suggesting an apparent degree
580 of cohesion, whereas they come from upper material that is not very cohesive and friable (Fig.
581 14c).

582

583 *Geology beneath the lander*

584

585 Thanks to the articulation of the arm, the IDC camera was able to acquire images under the
586 lander (Fig. 15) with sufficient precision to create a mosaic of ortho-rectified images on a digital
587 model of spatial resolution of $2\text{mm}\cdot\text{pixel}^{-1}$ (Fig. 16). The first surprise is the presence of two
588 large rocks that the lander was able to avoid during its landing (Fig. 15a). Both boulder/cobble-
589 sized rocks, called “Ace of spades, ~30 cm wide” and “Turtle, ~20 cm wide” by team
590 (Golombek et al., 2020), show a sub-equant shape with sub-angular edges. They have dark-
591 grey color and no mineral texture is visible at the IDC resolution, suggesting that they are
592 composed of volcanic material. The “Turtle” cobble displays a relatively dark, wavy top
593 surface that can be interpreted as a lava-corded surface or a surface shaped by the wind
594 (ventifacts) suggesting an aeolian abrasion (Fig. 15b). As observed on the workspace area,
595 several light-toned pebbles show planar-facets characteristics of wind abrasion (wind-faceted
596 pebbles) (Fig. 15c, e).

597 The IDC images display the partial sinking of the two front feet of the lander in a loose
598 material, showing evidence for slight sliding into place, creating a bulge in the ~south trending
599 and a depression on other side (Fig. 15c, d). In spite of the loose material, the feet of the lander
600 were able to stabilize, probably thanks to a more load-bearing sub-surface material.

601 During the landing, the retrorockets disturbed the surface under the lander, excavating up to
602 ~10 cm deep, ~50 cm-in-diameter pits providing thus views into subsurface materials and their
603 physical properties (Fig. 15a). The sub-surface material is mainly composed of dark-toned
604 aphanitic pebbles within a reddish finer-grained matrix (Golombek et al., 2020).

605 In the very shallow depression d3 (Fig. 15d and f), the sub-surface is also composed of sub-
606 angular pebbles, arranged in layers, within a reddish fine-grained matrix (Ansan et al., 2019).
607 But a few pebbles show a different texture and color, notably pebble made up of light-toned,
608 millimeter-sized, prismatic elements within a darker homogeneous matrix whose
609 elements/crystals are not visible at the IDC resolution. These prismatic elements could

610 correspond to feldspar minerals (phenocrysts) within a microlitic to microgranular matrix (Fig.
611 15g), suggesting a longer crystallization time. These pebbles would come from volcanic
612 material requiring longer crystallization time, i.e. deeper magmatic sources.

613 Based on the mosaic of ortho-rectified IDC images (Fig. 16a), a map of clasts present at the
614 surface (excluding the inner pit surfaces due to lack of stereo images in these areas) has been
615 performed taking into account their shape, using the same methodology as on the workspace
616 area. The median size of the clasts under the lander is 6.5 mm except the two cobbles, and they
617 are relatively sub-equant (Fig. 16b, c) over the mapped area, while the size of clast increases
618 near the pits with a mean of 13 mm (Fig. 16d), which suggests that these clasts are ejected clasts
619 due to their coarse size.

620 Using both ortho-rectified IDC images and DEMs, a detailed stratigraphy of the pits is made.
621 The ~8 cm deep depression d2, located in the forward part under the lander between its two
622 feet, shows three sub-horizontal superimposed units (Fig. 17), from top to down: R0) ~2 cm
623 thick unit composed of small pebbles-granules mixed reddish fine-grained matrix showing a
624 gentle surface slope of 10°, suggesting that this material is relative loose; R1) ~2 cm thick, very
625 fine-grained relatively reddish unit, showing lateral and vertical organization with resistant
626 laminae marked by a bench (black arrow in Fig. 17b) interstratified within a softer material
627 (Fig. 17b, d profile 2). Laterally, the softer material appears lighter (white arrow in Fig. 17b)
628 within a small scalloped depression topped with a resistant laminae well marked in topographic
629 profile 1 (Fig. 17d). These resistant laminae would have a higher degree of cohesion than the
630 softer material. They might be indurated by a cement, suggesting the local possible presence
631 of duricrust at depth of 2 cm below the surface; R4) ~3 cm thick bedrock, composed of poorly
632 sorted dark-toned, aphanitic pebbles within loose, fine-grained, reddish matrix. Note that the
633 R0 unit would extend laterally to the eastern lander footpad in which it is partially buried.

634 Material R1 would have stopped the footpad sinking and maintained its stability through its
635 greater load-bearing.

636 The ~50cm-in-diameter, >10 cm deep pit P1 located in the northeast part beneath the lander
637 (Fig. 15a) shows a very different morphology from the previous one. It is bordered by three
638 superposed clastic units (Fig. 18), from top to bottom: R2) ~3 cm thick unit composed of sandy
639 to poorly sorted, sub-angular to angular, pebble material; R3) ~2-6 cm thick unit composed of
640 poorly sorted, sub-equant, angular, >4cm wide pebbles. Some pebbles are longer than thick
641 (white arrow), suggesting that they are pieces of a larger pebble broken vertically. This thick
642 unit has a steep slope, greater than the angle of repose, up to 60°–86° (Fig. 18c) which can be
643 explained either by the arrangement of pebbles such as dry stone walls, or by the presence of
644 cement forming a sedimentary breccia. In the absence of better image resolution and chemical
645 analysis, it is not possible to conclude; R4) >3 cm thick unit of cohesionless, poorly sorted, sub-
646 angular pebbles within a fine-grained matrix. Note that the left side of the pit collapsed with a
647 very small slope of 15° eastward, suggesting that the upper layer R2 at least is no cohesive.

648 The third shallower ~50 cm-in-diameter pit P2 located in the northwest part beneath the
649 lander (Fig. 19) shows only to two units, from top to bottom: R2) sandy to poorly sorted, sub-
650 angular, gravel material and R3) poorly sorted, sub-angular pebbles arranged in a ~5 cm thick,
651 sub-horizontal unit. Many pebbles are longer than wide (white arrows), with their longer side
652 arranged sub-vertically and parallel to each other, suggesting that they have been sharply broken
653 either by the retro-rockets. Some large clasts have been ejected out of the pit (white arrow in
654 the left foreground, Fig. 19a), suggesting that this thick unit is composed of cohesionless, 5 cm
655 wide clasts, despite the relatively steep slope on the northern pit side. Note firstly that this unit
656 R3 is in continuity with that observed in depression P1, suggesting that these large pebbles are
657 not indurated but rather arranged like dry stone walls giving them a great slope stability.

658 Secondly, this unit would be sub-horizontal with a dip of $\sim 2^\circ$ toward SSE, using its spatial
659 correlation of upper boundary the in DEM.

660

661 **5. Stratigraphy in the Homestead hollow**

662

663 As we saw previously the NW part of Homestead hollow is filled by clastic material,
664 dominated by sand size grains. From all observations acquired in the workspace and beneath
665 the lander, a schematic sub-surface stratigraphy is proposed from lander to HP³ location (Ansan
666 et al., 2019), from top to bottom (Fig. 20a): i) a thin dust layer, probably $<$ few microns, with
667 cobbles and small boulder (Turtle and Ace of Spades), pebbles and granules at the surface; ii)
668 a few cm-thick unit consisting of light-toned, cohesionless, sand or smaller (<1 mm) grains. This
669 material was sculpted into $<$ cm deep troughs and ridges radial to the lander by the descent
670 rockets; iii) a possibly fine-grained indurated unit, called duricrust, at least in shallow
671 depression d2 in front the lander, showing lateral variations of thickness (ranging from a few
672 mm in front of lander up to ~ 2 cm beneath the lander). Laterally, a coarse-grained material (i.e.
673 composed of poorly-sorted, angular to sub-rounded dark-toned clasts, ranging from granules to
674 pebbles contained in lighter-toned, finer-grained (i.e. <0.5 mm) matrix) is present within
675 depression d3 near the western footpad; iv) a $\geq \sim 5$ cm-thick, cohesionless, granular material
676 comprised of a likely sandy matrix with poorly sorted clasts of sub-angular, dark-toned pebbles
677 are present with different lateral arrangement due to the proportional amount of clasts. In the
678 depression d2, the sandy matrix seems more important while it is almost absent in the pits (P1
679 and P2) in the back of the lander. This suggests that all stratigraphic units are spatially
680 distributed in lens-shaped features.

681 By plotting the different stratigraphic columns established from the ortho-rectified images
682 and DEM on the local map (Fig. 20b) and using the stratigraphic relationships, we notice that

683 the units located under the lander are made of coarser clastic materials (pebbles) than those
684 located in the workspace. These units reinforce the small slope on which the lander touched
685 down. The finer material distributed within the workspace show a variety of stratified grain
686 sizes. A geologic cross-section shows the spatial distribution of the different units between the
687 pit P1 under the lander and the indentation made at HP³ (Fig. 20c), with lens-shaped deposit.
688 Unfortunately it is difficult to deduce what type of clastic material is under the first few
689 centimeters of sand at HP³ location. We can assume that it would be a mixture of granules and
690 small gravels in a relatively porous sand matrix which has allowed the penetration of the mole
691 over the first ~30 cm of depth.

692 At the scale of Homestead hollow, the surficial clastic material shows a great variety of grain
693 sizes, ranging from cobbles to dust, with a dominant sandy size, distributed in sub-horizontal,
694 meter long, centimeter thick lens-shaped features, at least in its NW embankment area. The
695 geometry of these clastic materials suggests a sedimentary origin, at least for fine-grained
696 material transported by wind. For coarser clasts, their shape suggests that they have undergone
697 very short ground transport. Their spatial accumulation suggests that they came from nearby
698 impact ejected rocks, with vertical breaks created when they re-impacted the ground. However,
699 those at the surface of the depression were subjected to wind abrasion by the sand particles after
700 their ejecta fall, forming a residual lag (see Grant et al., 2020).

701 Based on the analysis of orbital data, the maximum thickness of the surficial clastic material
702 without boulders would be 2.5 m, using the crater morphometry relationships (Sweeney et al.,
703 2018) for no rocky ejecta 30 m-in-diameter impact craters, corresponding to the crater size
704 beyond which the impacts excavated the volcanic bedrock within a one-kilometer radius of the
705 landing site. If we assume that Homestead hollow is a 27 m-in-diameter, degraded impact
706 crater, the maximum thickness of fine-grained clastic material would be ~2.2 m, using crater
707 morphometry relationship for pristine small impact craters (Sweeney et al., 2018) up to 3 m

708 from model of crater shape evolution (Warner et al., 2020). Based on in situ data, the thickness
709 of clastic material is not constrain beyond a depth of ~10 cm, however the <meter-scale hollows
710 viewed in the smoother part of Homestead hollow are surrounded by small sandy rims (Fig. 6c)
711 whereas those, in rockier part of Homestead hollow and its boundary, are ringed by pebbles and
712 cobbles (Fig. 6a and 8).

713 Beyond this maximum meter-scale thickness of fine-grained material, the Early Amazonian,
714 fractured, layered lava flows would be present, as suggested by >50m-in-diameter rocky impact
715 craters surrounding the landing site, from which remnant ejected boulders at the southern
716 boundary of Homestead hollow could come from (Fig. 21).

717

718 **6. Discussion**

719

720 In this section, we will discuss about the nature and preservation of bedrock, the nature and
721 processes at the origin of surficial unit (regolith).

722

723 *Volcanic bedrock and clasts*

724

725 The InSight landing area is characterized by Early Amazonian, widespread, <60m thick,
726 volcanic flows, whose morphologic elements, such as lobate fronts, are well-preserved, despite
727 their age of 2.6 Ga. Underneath them, >500 m layered dark-toned material have been identified
728 in the inner walls of >2km large impact craters, interpreted as superimposition of volcanic
729 flows, dated of Early/Late Hesperian, from orbital data. The surface retention age, at InSight
730 landing, is consistent with previous regional chronology of Elysium Planitia and Elysium Mons,
731 for which the emplacement of the main edifice occurred at the latest 3.5 Ga ago and the
732 emplacement of major Elysium planitia occurred from 3.7 to 3.0 Ga with locally very young

733 volcanic events such as those in Central Elysium planitia (e.g. Werner, 2009; Vaucher et al.,
734 2009)

735 Although the area is quite close to Elysium Mons, their relative regular layered organization
736 suggests that they formed by fissural magmatic processes, as observed in Deccan traps on Earth.
737 Due to their large extension and morphological elements, these lavas could be composed of
738 relatively low viscosity flood basalts, as observed in Hesperian volcanic regions on Mars, such
739 as Lunae and Hesperia Planitiae (Carr, 2006; Hartmann, 2005; Werner, 2009). This is supported
740 by visual analysis of the large ejected clasts present on the surface of Homestead hollow and
741 under the lander, showing a majority of dark clasts with no mineralogical texture (aphanitic at
742 ~0.5 mm IDC scale) and no vugg, relatively resistant to wind erosion, typical of basaltic lava
743 flows. Nevertheless, some large clasts show a light-grey color with an aphanitic texture that
744 may correspond to andesites. In addition, a few clasts show a different texture and color, with
745 light-toned prismatic minerals that may be feldspars within a darker matrix (Fig. 15g),
746 suggesting they would come from deeper magmatic sources or lava flows with distinct
747 chemistry. These clasts could have been ejected from nearby craters sampling deeper section
748 of the volcanic flows. In absence of chemical and mineralogical analytical instruments, we
749 cannot conclude definitively about their nature. The dominant type of rocks shows that this
750 region was characterized by homogeneously basaltic, effusive flows.

751 Although undergoing cratering since 3.6 Ga, the volcanic materials as a whole have
752 preserved their overall layered structure, not developing a megaregolith (i.e. a larger-scale
753 disrupted crustal structure by impacts in reference to that on the Moon, e.g. Hartmann, 1973;
754 Short & Foreman 1972, Hôrz et al. 1976) at the km scale.

755

756

757

759

760 Since the last volcanic flows dated of 2.6 Ga, the region has been cratered forming a majority
761 of small craters less than 200 m-in-diameter. These craters and those down to 50 m-in-diameter
762 are surrounded by rocky ejecta coming from disruption of lava flows by impacts. The ejected
763 clasts could comprise not only piece of lava flows; as mentioned previously, but also meteorite
764 fragments and impactites consisting of shocked and shock-melted materials in larger, angular
765 clasts. In Homestead hollow, none of these types of clasts have been identified, unlike those
766 found within Gale Crater (Yingst et al., 2013), even if it is not ruled out in the Homestead home
767 surroundings.

768 For the smaller <200 m-in-diameter craters, the ejecta appear to be composed of finer
769 material, suggesting that they could mainly result from ejecta reworking by impacts at the origin
770 of the formation of "lunar regolith". Indeed, on the Moon, impacts have been fragmented the
771 original surface and distributed it as ejecta, which intermixed with successive cratering products
772 (fragmental layer of broken, melted, and otherwise altered debris). By iterative process, the
773 numerous small down to micro-impacts only disturbed and mixed (gardened) the regolith layer
774 already present, and the regolith thickness increased more slowly (McKay et al., 1991). The
775 lunar regolith consists thus of clasts <1 cm in size although larger cobbles and boulders are
776 commonly found at the surface. This unconsolidated, heterogeneous and fragmented lunar
777 material is generally about 4–5 m thick in the mare but may average about 10–15 m in older
778 highland regions (Oberbeck & Quaide, 1967, 1968; McKay et al., 1991).

779 However, the presence of such a "lunar-type" regolith is quite inconceivable on Mars due to
780 the presence of an atmosphere, coupled with diurnal and seasonal thermal cycles, which
781 prevents or reduces micrometeoroid penetration to the surface. In addition, due to the existence
782 of a dynamic hydrosphere in early Mars's history, there is evidence for the action of liquid

783 water in terms of weathering, erosion and deposition of sediments, whether intermittent or
784 continuous, as well as the formation of sedimentary rocks (e.g. Squyres et al.2004, Malin et
785 Edgett, 2000; Dromart et al., 2007; Ansan et al., 2011; Grotzinger et Milliken, 2012). In
786 addition, the thin Martian atmosphere has driven wind systems that have resulted in aeolian
787 transport and deposition (e.g., dust storms (Cantor, 2007), dunes and ripples (e.g. Kocurek &
788 Ewing, 2012)), which continue to the present day. In summary, not only Martian surface
789 materials may comprise disaggregated precursor rocks, but they will also comprise
790 unconsolidated materials derived from fluvial, lacustrine, aeolian, and glacial activity that
791 postdate and drape earlier impact-dominated processes of Noachian (pre-3.7Ga) age. The
792 Martian regolith (i.e. the uppermost unconsolidated, fragmented material resting on bedrock) is
793 therefore more complex than that of the Moon.

794 In the equatorial region of western Elysium Planitia, no evidence of hydrological and glacial
795 activity has been identified from orbital data. Only dunes, wind streaks, and dust devils give
796 evidence of relatively old wind activity, still active until today. In Homestead hollow, the
797 presence of sand and dust attests its partially infilling by aeolian process, even if no aeolian
798 features such as sand sheet, sand drift, ripples and dunes, nor internal texture (e.g. cross-
799 bedding) has been observed. The source of this sandy material could be attributed either to
800 local sources such as the remobilization of surface granular material from the regolith itseft
801 (Bourke et al., 2004; Fenton, 2005), the walls of deeper impact craters within layered lava flows
802 (Tirsh et al., 2011), or more regional sources such as ashes and sedimentary material within
803 Medusae Fossae formation (Mandt et al., 2008; Zimbelman et Griffin, 2010). Although dust
804 covers the whole planet, the source of dust storms is usually found in the southern hemisphere
805 in areas such as Hellas, Argyre and Solis within a latitudinal zone ranging from 20° to 50°S.
806 Dust is then transported via regional to global dust storms preferentially occurring during

807 southern spring to summer (e.g., Martin and Zurek, 1993; McKim, 1996) and settled with
808 microscopic thickness over the entire Martian surface.

809 Although the measured grain size determined at the landing site is ≥ 0.5 mm in diameter due
810 to the resolution of the IDC camera at close range, it is likely that the grain size is very smaller
811 than ~ 100 μm , due to their low mobility during wind gusts. In reference to previous robotic
812 missions (e.g. MER and Curiosity rovers), the size of fine grains was considered to be around
813 $200 \mu\text{m} \pm 50$ (fine sand) before landing (Golombek et al., 2017). However, the granulometry
814 of the Rocknest sand shadow in Gale crater (Minitti et al., 2013), considered as a representative
815 surficial regolith sample on Mars, has $< 10\%$ of $0.5\text{--}2$ mm-in-diameter grains, $40\text{--}60\%$ of grains
816 between $100\text{--}150 \mu\text{m}$, and $30\text{--}50\%$ of finer grains (i.e. $< 31 \mu\text{m}$, because smaller grain size
817 could not be resolved by MAHLI imager (Edgett et al., 2012)) would be similar within
818 Homestead home. Although the size of the dust grains has not been measured directly on Mars,
819 it is probably less than a few microns. Combining optical and atomic force microscopy, grains
820 less than $4 \mu\text{m}$ in diameter would be found in regolith at Phoenix landing site (Pike et al., 2011).
821 So, the grains ranging from coarse sand to dust could be present within Homestead hollow, in
822 various proportions, as found in other Martian regolith samplings.

823

824 *Lithology and structure of clasts*

825

826 In reference to geological context, the regolith would have a basaltic composition, as found
827 in others landing sites (Yen et al., 2005; Ming and Morris, 2017), derived from a globally
828 basaltic crust (McSween et al., 2009). As within regolith in Gale crater, it cannot be ruled out
829 that the fine grain component comprises 50% glass fragments mixed in crystalline phases and
830 a dust component, with a mineralogy dominated by feldspar, pyroxene, olivine, with minor
831 magnetite, anhydrite, hematite and their weathered derivatives, as revealed by the CheMin and

832 APXS instruments on the Mars Science Laboratory (MSL) Curiosity rover (Bish et al., 2013;
833 Blake et al., 2013; Dehouck et al., 2014; Achilles et al., 2017). The glass component would
834 contain a water abundance of 1.5 to 3 weight percent, which is supported by the isotopic
835 analyses, suggesting an atmospheric source of water (Leshin et al., 2013). The possible
836 presence of minor amount of sulfates and chlorides at Homestead hollow could explain partly
837 the presence of soft, light-toned, fine-grained material observed in the depression d2 underneath
838 the lander (R1 in Fig. 17b). In addition, the magnetite content could be higher than that
839 analyzed in Gale Crater, if it is assumed that the particles came from airborne magnetic dust
840 captured by magnets on the board of MER (Bertelsen et al., 2004) and from the local abrasion
841 of volcanic materials in the region. This could give it different physical properties from those
842 of other regoliths studied at different landing sites.

843 At the meter scale, the lens-shaped organization of the different sub-surface clastic
844 components was discovered thanks to the artificial depressions created by the lander
845 retrorockets and the HP³ mole (Fig. 20, 21). The clastic lenses have meter horizontal extent
846 and a thickness of ten centimeters, which gives a strong spatial heterogeneity into clastic
847 deposits. This could explain the difficulty of the HP³ mole penetration in the subsurface.
848 InSight landed on the inner gentle slope of Homestead hollow, reinforced by a sub-surface more
849 than 10 cm thick cluster of ejected pebbles/cobbles, whose southeastward extension could
850 continue deeply until the location of HP³. The thin-layered, heterogeneous fine-grained
851 material, found at HP³ location, would be the core deposit of the hollow center with spatial
852 heterogeneities due to the differentiated content of dust and sand. This spatial organization will
853 be refined by the data acquired by the seismometer SEIS during its mission extending.

854 In summary, the InSight landing site is characterized by aeolian sediments (sand and dust)
855 trapped in impact craters, hollows and intercrater areas, interstratified into ejected clasts and

856 ejecta blankets (this study, Golombek et al., 2020; Grant et al., 2020; Warner et al., 2020) rather
857 than a *sensus stricto* impacted-related regolith (i.e. *in situ* fragmented material).

858

859 *Cohesion, lithification of fine-grained material at Homestead hollow?*

860

861 On Earth, diagenesis is typically divided into two processes: lithification and epigenesis.
862 Lithification is the primary conversion of sediment to sedimentary rock. This involves
863 compaction (via burial), the expulsion of fluids, the reduction of porosity, and the precipitation
864 of a binding medium (cement). There may be further grain growth, and replacement and
865 generation of secondary interstitial phases, process called epigenesis.

866 On Mars, the contribution of sedimentary processes is regionally significant. In many
867 places, the surface consequently encompasses a variety of fine clastic components identified at
868 landing sites, such as dust cover, sandy bedforms, and more cohesive features as bedform
869 armors and "cemented" or "indurated" sand, usually called duricrust. Due to their relative
870 cohesion, sand grains bonded to each other with/o fine matrix were interpreted as glued together
871 by cement, which would imply the presence of a liquid fluid transporting soluble salts or
872 oxides/hydroxides. As observed in Gale crater and Gusev crater, the presence of such processes
873 might have been helped by hydrothermal fluid containing sulfates and Fe-oxides (e.g. Wang et
874 al., 2006; Yen et al. 2008; Blake et al., 2013). In other places in Gusev crater, crusty, flaky,
875 cemented, and cohesive materials partly consisting of composite grains (millimeter to
876 centimeter aggregates of clast smaller than $\sim 30 \mu\text{m}$) broke with clean-cut fractures when
877 Mossbauer Spectrometer was applied to their surface (Cabrol et al., 2014). This behavior was
878 also observed in fined-grained surface material within basalt plains unit of Gusev, in which
879 trenches made by rover wheels, showing the material frequently behaves like a sheet of
880 indurated fine-grained material a few mm thick (Arvidson et al., 2004, Herkenhoff et al., 2004).

881 The very fine-grained subsurface material showed also modest degrees of cohesion, with values
882 of <1 kilopascal, perhaps resulting from electrostatic forces or a modest degree of cementation
883 (Arvidson et al., 2004).

884 The presence of cement remains debated within Homestead hollow. Near the lander, the ~2
885 cm thick, very fine-grained relatively reddish unit R1 shows variations in the lateral and vertical
886 organization with resistant sandy laminae marked by a bench (black arrow in Fig. 17b)
887 interstratified within a softer brighter material (Fig. 17b, d profile 2), suggesting a variation of
888 degree of cohesion in materials buried at a depth of 2 cm. This cohesion could result from the
889 interaction between the S- and Cl-rich components of the granular material and the atmospheric
890 water vapor absorbed at the surface of the grains, occurring during recent changes of Mars
891 obliquity, as observed in Spirit hollows within Gusev crater (Weitz et al., 2020). But without
892 chemical analysis at InSight landing site, the question remains open.

893 Within Homestead hollow, the surficial granular material is composed of very fine grains
894 mixed within coarse sand and granules, at HP³ location at least. Its relative low degree of
895 cohesion is supported by the grain flows along the flat planar collapsing pit wall (Fig. 13, 14).
896 Some aggregates of coarse sands within a very fine grained matrix were also observed after
897 several tests of HP³ hammering. Although the presence of cement cannot be ruled out, the
898 amount of water vapor in the current atmosphere at ground level near the equator appears to be
899 very low, in comparison to that measured at higher latitude and altitude (e.g. Vincendon et al,
900 2011; Federova et al., 2018; Savijarvi et al., 2019; Aoki et al., 2019), which would inhibit
901 chemical reactions at the surface-atmosphere boundary.

902 To explain the apparent cohesion of the granular material near HP³, the most relevant
903 parameters would be the very fine size of the particles, their shape, their composition and the
904 vibration or compaction processes generated during the HP³ hammering. For parameters
905 associated with grains, they remain unknown due to the absence of microscopic optics and

906 chemical and mineralogical analysis instruments in the InSight mission. However, the amount
907 of dust contained in the granular material could greatly influence this cohesion. On Mars, the
908 dust is composed of charged-particles (e.g. Bertelsen et al., 2004; Ardivison et al., 2006),
909 promoting the electrostatic cohesion. The compaction induced by hammering tests would have
910 favored the apparent cohesion of the fine-grained material thanks to electrostatic forces, while
911 keeping its weakness. The process would be all the most efficient if we consider the possible
912 important amount of dust mixed to sand. Coupled to compaction/vibration, the effect of lower
913 gravity on cohesive behavior on fine powders would be greater than on Earth (Walton et al.,
914 2007), which would promote the apparent cohesion. This apparent cohesion induced by the
915 vibrations/compaction of the HP³ hammering would be localized not only around the mole but
916 also to the whole surficial (cm-scale) granular unit of the hollow, inhibiting the formation of
917 dust devils in the field of view of the cameras, while their traces are observed a few hundred
918 meters from the lander.

919

920 **7. Conclusion**

921

922 Homestead hollow is a unique place of Mars, in which InSight lander touched down in 2018.
923 The combination of orbital and in situ data enabled to understand the structure of upper crust
924 over the first hundreds meters of depth. It consists of two major units: 1) the bedrock unit
925 composed of 60 m thick, Early Amazonian lava flows overlapping >500m thick Late Hesperian
926 layered volcanic floods and 2) ~3 m thick, surficial unit consisting of superimposition of lens-
927 shaped clastic features filling the hollow. The latter corresponds to the Martian regolith, whose
928 formation processes are cratering, aeolian sedimentation and thermal alteration to a lesser
929 extent, at Insight landing site, and it differs from the lunar (cratering) and terrestrial (in situ
930 alteration and biological activity) regoliths by sedimentary processes.

931 This is the first time that the lens-shaped structure of the Martian regolith has been observed
932 and analysed. In Homestead hollow, the lens-shaped features are composed of volcanic \leq
933 boulder-sized clasts ejected by nearby impacts interstratified within aeolian sedimentary
934 materials essentially composed of loose centimeter pebbles, granules, sand and dust at near-
935 surface. The surficial clastic unit did not appear to have been transformed by early diagenetic
936 processes at least over the first 10 cm of depth, since the fine sandy eolian granular material is
937 characterized by high porosity and a very low cohesion. Then, as on the entire Martian surface,
938 the area was subjected to aeolian exhumation, leaving coarse clasts in place and forming a
939 residual lag.

940

941 **Acknowledgments.** We thank the French agencies, CNES and CNRS, which have supported
942 and funded this work. We thank IPGP and JPL employees for the logistics and the very good
943 hospitality during the operations of the mission.

944

945

946 **References**

- 947 Abarca, H., Deen, R., Hollins, G. et al., 2019. Image and Data Processing for InSight Lander
948 Operations and Science. *Space Sci. Rev.* 215, 22, doi:10.1007/s11214-019-0587-9.
- 949 Achilles, C. N., Downs, R. T., Ming, D. W., Rampe, E. B., Morris, R. V., Treiman, A. H., et
950 al., 2017. Mineralogy of an active eolian sediment from the Namib dune, Gale crater, Mars.
951 *J. Geophys. Res. Planets*, 122, 2344–2361, doi:10.1002/2017JE005262.
- 952 Aoki, S., Vandaele, A. C., Daerden et al. , 2019. Water vapor vertical profiles on Mars in dust
953 storms observed by TGO/NOMAD. *J. Geophys. Res.*, 124, 3482-3497, doi:10.1029/
954 2019JE006109.
- 955 Allemand, P . and P. Thomas, 1992. Modèle fragile des rides martiennes contraint par la
956 géométrie de surface. *C. R. Acad. Sci. Paris, Sér. II*, 215, 1397-1402.
- 957 Ansan, V., E. Hauber, M. Golombek et al., 2019. InSight landing site: subsurface stratigraphy
958 and implications for formation processes. 9th International Mars Conference, Pasadena, USA
- 959 Ansan, V et al., 2015. Western Elysium Planitia, What is regional geology telling us about sub-
960 surface? in *InSight Science Team Presentation*, Zurich, Switzerland, September 5–9, 2015.
- 961 Ansan, V., D. Loizeau, N. Mangold, S. Le Mouélic, J. Carter, F. Poulet, G. Dromart, A. Lucas,
962 J-P. Bibring, A. Gendrin, B. Gondet, Y. Langevin, Ph. Masson, S. Murchie, J. Mustard, G.
963 Neukum, 2011. Stratigraphy, mineralogy, and origin of layered deposits inside Terby crater,
964 Mars. *Icarus*, vol. 221, 273-304, doi:10.1016/j.icarus.2010.09.011.
- 965 Arvidson, R. E., et al. 2006. Overview of the Spirit Mars Exploration Rover Mission to Gusev
966 Crater: Landing site to Backstay Rock in the Columbia Hills, *J. Geophys. Res.*, 111, E02S01,
967 doi:10.1029/2005JE002499.
- 968 Arvidson, R. E., et al. 2004. Localization and physical properties experiments conducted by
969 Spirit at Gusev Crater, *Science*, 305(5685), 821–824, doi:10.1126/science.1099922.

970 Baker, M., C. Newman, M. Lapotre et al., 2020. Aeolian activity at the MSL and InSight landing
971 Ssites. ICAR, Swakopmund, Namibia.

972 Baker, C. Newman, C. Charalambous, M. Golombek, A. Spiga, D. Banfield, M. Lemmon, M.
973 Banks, J. Garvin, J. Grant, K. Lewis, V. Ansan, N. Warner, C. Weitz, S. Wilson, 2020. The
974 modern aeolian environment at Homestead hollow, Mars. Submitted in J.Geophys. Res.

975 Balme, M., R. Greeley, 2006. Dust devils on Earth and Mars. Rev. Geophys. 44, 3,
976 2005RG000188, doi: 10.1029/2005RG000188.

977 Banerdt, W.B., Smrekar, S.E., Banfield, D. et al. Initial results from the InSight mission on
978 Mars. 2020. Nat. Geosci. 13, 183–189, doi. :10.1038/s41561-020-0544-y.

979 Banerdt, W.B., et al., 2013. InSight: a discovery mission to explore the interior of mars Lunar
980 Planet. Sci. Conf. (Lunar and Planetary Institute, Houston, 2013) Abstract #1915

981 Banfield, D. et al., 2020. An overview of the initial results on atmospheric science from InSight
982 measurements. Nature Geoscience, vol. 13, 190-198, Special issue, doi: 10.1038/s41561-
983 020-0534-0.

984 Banfield, D. et al., 2019. InSight Auxiliary Payload Sensor Suite (APSS). Space Sci. Rev. 215,
985 4, doi:10.1007/s11214-018-0570-x.

986 Balme, M., D. C. Berman, M. C. Bourke, *and* J. R. Zimbelman, 2008. Transverse Aeolian
987 Ridges (TARs) on Mars, Geomorphology, 101, 703–720,
988 doi:10.1016/j.geomorph.2008.03.011.

989 Bertelsen, P., et al., 2004. Magnetic properties experiments on the Mars Exploration Rover
990 Spirit at Gusev Crater. Science, 305, 827–829.

991 Bibring, J. P., Langevin, Y., Gendrin, A., Gondet, B., Poulet, F., Berthé, M., et al., 2005. Mars
992 surface diversity as revealed by the OMEGA/Mars Express observations. Science, 307,
993 5715, 1576–1581, doi:10.1126/science.1108806.

994 Bryan, W.B., 1973. Wrinkle-ridges as deformed surface crust on ponded mare lava. *Geochim.*
995 *Cosmochim. Acta Suppl.* 1, 93–106.

996 Bish, D.L., Blake, D.V., Vaniman et al., 2013. X-ray diffraction results from Mars science
997 laboratory: mineralogy of rocknest at Gale Crater. *Science* 341, 1238932,
998 doi:10.1126/science.1238932.

999 Blake D.F. et al, 2013. Curiosity at Gale Crater, Mars: Characterization and Analysis of the
1000 Rocknest Sand Shadow. *Science* 341, doi: 10.1126/science.1239505.

1001 Bourke, M.C., Bullard, J.E., Barnouin-Jha, O.S., 2004. Aeolian sediment transport pathways
1002 and aerodynamics at troughs on Mars. *J. Geophys. Res.* 109,
1003 doi.org/10.1029/2003JE002155.

1004 Cabrol, N. A., et al. (2014), Sands at Gusev Crater, Mars, *J. Geophys. Res. Planets*, 119, 941–
1005 967, doi:10.1002/2013JE004535

1006 Cantor, B.A., 2007. MOC observations of the 2001 Mars planet encircling dust storm. *Icarus*
1007 186, 60–96. doi:10.1016/j.icarus.2006.08.019.

1008 Cantor, B. A., K.M. Kanak, K. S Edgett, 2006. Mars Orbiter Camera observations of Martian
1009 dust devils and their tracks (September 1997 to January 446 2006) and evaluation of
1010 theoretical vortex models. *JGR Planets*, 111 (12), 1-49, doi: 10.1029/2006JE002700.

1011 Carr, M. H., 2006. *The Surface of Mars*. New York: Cambridge University Press.

1012 Chapman, C. R. and W.B. McKinnon, 1986. Cratering of planetary satellites. In *Satellites* (eds.
1013 J. Bums and M. Matthews), pp. 492-580. Univ. Arizona Press, Tucson, Arizona.

1014 Charalambous, C., 2015. On the evolution of particle fragmentation with applications to
1015 planetary surfaces. Ph.D. Thesis (Imperial College, London).

1016 Charalambous, C. et al., 2020. Aeolian changes at the InSight landing site and multi-instrument
1017 observations. 51st LPSC, Houston, USA.

1018 Charalambous C., McClean J. B., Baker M. et al., 2020. Aeolian Changes at the InSight Landing
1019 Site: Multi-instrument Observations. Submitted in GRL.

1020 Chicarro A.F., P. H. Schultz and P. Masson, 1985. Global and Regional Ridge Patterns on Mars.
1021 *Icarus* 63, 153-174.

1022 Christensen, P.R., B.M. Jakosky, H.H. Kieffer, M.C. Malin, H.Y. McSween Jr., K. Nealson,
1023 G.L. Mehall, S.H. Silverman, S. Ferry, M. Caplinger, M. Ravine, 2004. The Thermal
1024 Emission Imaging System (THEMIS) for the Mars 2001 Odyssey mission. *Space Sci. Rev.*
1025 110, 85-130.

1026 Christensen, P. R., Bandfield, J. L., Smith, M. D., Hamilton, V. E., & Clark, R. N., 2000.
1027 Identification of a basaltic component on the Martian surface from thermal emission
1028 spectrometer data. *J. Geophys. Res.*, 105, E4, 9609–9621, doi:10.1002/ 1999JE001127.

1029 Connerney, J. E. P. et al., 2015. First results of the MAVEN magnetic field investigation.
1030 *Geophys. Res. Lett.* **42**, 8819– 8827.

1031 Daubar, I. J. et al., 2016. Changes in blast zone albedo patterns around new Martian impact
1032 craters. *Icarus* 267, 86-105, doi:10.1016/j.icarus.2015.11.032.

1033 Dehouck, E., McLennan, S.M., Meslin, P.-Y., Cousin, A., 2014. Constraints on abundance,
1034 composition, and nature of X-ray amorphous components of soils and rocks at Gale Crater,
1035 Mars. *J. Geophys. Res.* 119, 2640–2657, doi:10.1002/ 2014JE004716.

1036 Dromart, G, Quantin, C, Broucke, O, 2007. Stratigraphic architectures spotted in southern
1037 Melas Chasma, Valles Marineris, Mars. *Geology* 35:343–366.

1038 Edgett, K. S., et al. (2012), Curiosity’s Mars Hand Lens Imager (MAHLI) investigation. *Space*
1039 *Sci. Rev.* 170, 259–317, doi:10.1007/s11214-012-9910-4.

1040 Fedorova, A., Bertaux, J.-L., Betsis, D., Montmessin, F., Korablev, O., Maltagliati, L., &
1041 Clarke, J. (2018). Water vapor in the middle atmosphere of Mars during the 2007 global dust
1042 storm. *Icarus*, 300, 440–457, doi:10.1016/j.icarus.2017.09.025.

1043 Fenton, L.K., 2005. Potential sand sources for the dune fields in Noachis Terra, Mars. *J.*
1044 *Geophys. Res.* 110, doi:10.1029/2005JE00243.

1045 Ferguson, R.L. et al., 2017. Analysis of Local Slopes at the InSight Landing Site on Mars. *Space*
1046 *Sci. Rev.* 211,109–133, doi:10.1007/s11214-016-0292-x.

1047 Forget, F. et al., 1999. Improved general circulation models of the Martian atmosphere from
1048 the surface to above 80 km. *J. Geophys. Res.* 104, 24155– 24176.

1049 Garvin, J.B., Sakimoto, S., Frawley, J., 2003. Craters on Mars: Global geometric 1142
1050 properties from gridded MOLA topography. In: Sixth International Conference on Mars,
1051 Pasadena, CA, USA, p. 3277.

1052 Geissler, P. E., 2014. The birth and death of transverse aeolian ridges on Mars. *J. Geophys. Res.*
1053 *Planets*, 119, 2583–2599, doi:10.1002/2014JE004633

1054 Giardini, D., Lognonné, P., Banerdt, W.B. et al., 2020. The seismicity of Mars. *Nat. Geosci.*
1055 13, 205–212, doi:10.1038/s41561-020-0539-8

1056 Golombek, M. P. et al., 2020. Geology of the InSight landing site on Mars: *Nature Comms.*,
1057 11, 1014, doi:10.1038/s41467-020-14679-1.

1058 Golombek, M. P. et al., 2018. Geology and physical properties investigations by the InSight
1059 Lander. *Space Sci. Rev.* 214, 84, doi:10.1007/s11214-018-0512-7.

1060 Golombek, M. P., D. M. Kipp, N. H. Warner et al., 2017. Selection of the InSight landing site.
1061 *Space Sci. Rev.* 1551, doi:10.1007/s11214-016-0321-9.

1062 Golombek, M.P. and R.J. Phillips, 2009. Mars tectonics. In *Planetary Tectonics*, chp. 5, edited
1063 by Thomas R. Watters and Richard A. Schultz, Cambridge University Press.

1064 Golombek, M.P., F.S. Anderson and M.T. Zuber, 2001. Martian wrinkle topography: Evidence
1065 for subsurface faults from MOLA. *J. Geophys. Res.* 106, E10, 23,811-23,821.

1066 Gómez-Elvira, J. et al., 2012. REMS: the Environmental Sensor Suite for the Mars Science
1067 Laboratory Rover. *Space Sci. Rev.* 170, 583–640.

1068 Grant, J. A., N. H. Warner, C. M. Weitz, M. P. Golombek, S. A. Wilson, M. Baker, E. Hauber,
1069 V. Ansan, C. Charalambous, N. Williams, F. Calef, W. T. Pike, A. DeMott, M. Kopp, H.
1070 Lethcoe, and M. Banks, 2020. Modification of Homestead hollow at the Insight landing site
1071 based on the distribution and properties of local deposits. *J. Geophys. Res.* accepted.

1072 Grant, J., N. H. Warner, C. M. Weitz, M. P. Golombek, S. A. Wilson, E. Hauber, V. Ansan, C.
1073 Charalambous, N. Williams, F. Calef, T. Pike, A. DeMott, M. Kopp, H. Lethcoe, 2019.
1074 Modification of homestead hollow at the insight landing site based on the distribution and
1075 properties of local deposits. 50th LPSC #1199, Houston, USA.

1076 Grotzinger, J. P., R. E., Milliken, 2012. The Sedimentary Rock Record of Mars: Distribution,
1077 Origins, and Global Stratigraphy, in *Sedimentary geology of Mars*, 1-49, eds Grotzinger, J.
1078 P., R. E., Milliken, SEPM special publication no. 102.

1079 Guzewich, S. D., Lemmon, M., Smith, C. L., Martínez, G., de Vicente-Retortillo, Á., Newman,
1080 C. E., et al., 2019. Mars Science Laboratory Observations of the 2018/Mars Year 34 Global
1081 Dust Storm. *GRL*, 46, 71–79, doi:10.1029/2018GL080839.

1082 Hartmann W. K. 1970. Preliminary note on lunar cratering rates and absolute time-
1083 scales. *Icarus* 12:131–133.

1084 Hartmann, W. K., 1973. Ancient lunar megaregolith and subsurface structure. *Icarus* 18, 634–
1085 639.

1086 Hartmann, W. K., 1995. Planetary cratering I . The question of multiple impactor populations:
1087 Lunar evidence. *Meteoritics* 30, 451-467.

1088 Hartmann, W. K., 2005. Martian cratering 8: Isochron refinement and the history of Martian
1089 geologic activity, *Icarus*, 174, 294– 320, doi:10.1016/j.icarus.2004.11.023.

1090 Hartmann, W. K., and Gaskell, R., 1997. Planetary cratering II. Studies of saturation
1091 equilibrium. *Meteoritics and Planet. Sci.* 32, 109-121.

1092 Hartmann, W. K., M. C. Malin, A. S. McEwen, M. H. Carr, L. A. Soderblom, P. Thomas, E.
1093 Danielson, P. James, and J. Veverka, 1999. Evidence for recent volcanism on Mars from
1094 crater counts. *Nature* 397, 6720, 586–589.

1095 Hauber, E., V. Ansan, C. Szczech, S. Adeli, M. Golombek, N. Warner, C. Charalambous, J.
1096 Grant, C. Weitz, and the InSight Geology Team, 2019. Geology of the InSight Landing Site,
1097 Mars: Initial Results. EPSC-DPS Joint meeting, Genève, Swithland.

1098 Herkenhoff, K. E., et al. (2004), Textures of the soils and rocks at Gusev Crater from Spirit's
1099 Microscopic Imager, *Science*, 305(5685), 824– 826, doi:10.1126/science.1100015.

1100 Hörz, F., Gibbons, R.V., Hill, R.E., Gault, D.E., 1976. Large-scale cratering of the lunar
1101 highlands: some Monte Carlo model considerations. *Proc. Lunar Sci. Conf.* 7, 2931–2945.

1102 Ivanov, B. A. (2001), Mars/Moon cratering rate ratio estimates, in *Chronology and Evolution*
1103 *of Mars*, edited by R. Kallenbach, J. Geiss, and W. K. Hartmann, pp. 87–104, Springer,
1104 Netherlands.

1105 Jaumann, R. et al., and the HRSC Co-Investigator Team, 2007. The High Resolution Stereo
1106 Camera (HRSC) experiment on Mars express: Instrument aspects and experiment conduct
1107 from interplanetary cruise through the nominal mission. *Planet. Space Sci.* 55, 928–952.
1108 doi:10.1016/j.pss.2006.12.003.

1109 Johnson, C. L. et al., 2020. Crustal and Time-Varying Magnetic Fields at the InSight Landing
1110 Site. *Nature Geoscience*, vol. 13, 199-204, Special issue, doi: 10.1038/s41561-020-0537-x.

1111 Johnson J. R. et al. (2014) ChemCam passive reflectance spectroscopy of surface materials at
1112 the Curiosity landing site, *Mars. Icarus* 249, 74-92.

1113 Kocurek G, Ewing RC. 2012. Source-to-sink: an Earth/Mars comparison of boundary
1114 conditions for eolian dune systems. *SEPM Spec. Publ.* 102,151–168.

1115 Langlais, B., Civet, F. & Thebault, E., 2017. In situ and remote characterization of the external
1116 field temporal variations at Mars. *J. Geophys. Res. Planets* 122, 110–123.

1117 Leshin, L.A., Mahaffy, P.R., Webster, C.R. et al., 2013. Volatile, isotope, and organic analysis
1118 of martian fines with the Mars curiosity rover. *Science* 341, 1238937,
1119 doi:10.1126/science.1238937.

1120 Lognonné, P. et al., 2020. Constraints on the shallow elastic and anelastic structure of Mars
1121 from InSight seismic data. *Nature Geoscience*, 13, 213-220, Special issue,
1122 doi:10.1038/s41561-020-0536-y

1123 Lognonné, P. et al., 2019. SEIS: Insight's Seismic Experiment for Internal Structure of Mars.
1124 *Space Sci. Rev.* 215, 12, doi: 10.1007/s11214-018-0574-6.

1125 Maki, J.N., Golombek, M., Deen, R. et al, 2018. The Color Cameras on the InSight Lander.
1126 *Space Sci. Rev.* 214, 105, doi:10.1007/s11214-018-0536-z.

1127 Malin, M.C., Edgett, K.S., 2000. Sedimentary rocks of early Mars. *Science* 290, 1927–1937,
1128 doi:10.1126/science.290.5498.1927.

1129 Malin, M.C. et al., 2007. Context Camera Investigation on board the Mars Reconnaissance
1130 Orbiter. *J. Geophys. Res.* 112, doi: 10.1029/2006JE002808.

1131 Mandt, K. E., S. L. de Silva, J. R. Zimbelman, and D. A. Crown, 2008. Origin of the Medusae
1132 Fossae Formation, Mars: Insights from a synoptic approach, *J. Geophys. Res.*, 113, E12011,
1133 doi:10.1029/2008JE003076.

1134 Mangold, N., P. Allemand and P.G.Thomas, 1998. Wrinkle ridges of Mars: Structural analysis
1135 and evidence for shallow deformation controlled by ice rich décollements, *Planet. Space*
1136 *Sci.*, 46, 345-356.

1137 Martin, L. J., and R. W. Zurek, 1993. An analysis of the history of dust activity on Mars. *J.*
1138 *Geophys. Res.* 98, 3221–3246, 1993.

1139 Maxwell, T.A., F. El-Baz, S.H. Ward, 1975. Distribution, morphology, and origin of ridges and
1140 arches in Mare Serenitatis. *Geological Society of America Bulletin*, v. 86, p. 1273-1278

1141 McEwen, A.S. et al., 2007. Mars Reconnaissance Orbiter's High Resolution Imaging Science
1142 Experiment (HiRISE). *J. Geophys. Res.* 112, E05S02. doi:10.1029/2005JE002605.

1143 McKim, R., 1996. The dust storms on Mars. *J. Br. Astron. Assoc.* 106, 185–200.

1144 Melosh, H.J., 1989. *Impact Cratering: A Geologic Process*. Oxford University Press, New
1145 York.

1146 McKay, D.S., Heiken, G.H., Basu, A., Blanford, G., Simon, S, et al. 1991. The lunar regolith.,
1147 in *Lunar Sourcebook: A User's Guide to the Moon*, edited by G. H. Heiken, D. T. Vaniman,
1148 B. M. French©1991, Cambridge University Press, chap. 7. pp. 285–356.

1149 Michael, G. G., 2013. Planetary surface dating from crater size–frequency distribution
1150 measurements: Multiple resurfacing episodes and differential isochron fitting, *Icarus*,
1151 226(1), 885–890.

1152 Michael, G. G., and G. Neukum, 2010. Planetary surface dating from crater size–frequency
1153 distribution measurements: Partial resurfacing events and statistical age uncertainty, *Earth*
1154 *Planet. Sci. Lett.*, 294(3), 223–229.

1155 Michael, G. G., T. Platz, T. Kneissl, and N. Schmedemann, 2012. Planetary surface dating from
1156 crater size–frequency distribution measurements: Spatial randomness and clustering, *Icarus*,
1157 218(1), 169–177.

1158 Minitti, M.E., Kah, L.C., Yingst, R.A. et al., 2013. MAHLI at the Rocknet sand shadow: science
1159 and scienceenabling activities. *J. Geophys. Res.* 118, 2338–2360, doi:10.1002/
1160 2013JE004426.

1161 Mueller, K. and M. Golombek, 2004. Compressional structure on Mars. *Annu. Rev. Earth*
1162 *Planet. Sci.* 32, 435–64, doi: 10.1146/annurev.earth.32.101802.120553

1163 Neukum G., K€onig B., and Arkani-Hamed J. 1975. A studyof lunar impact crater size-
1164 distributions.*The Moon*12:201–229

1165 Neukum, G., Jaumann, R., and HRSC Co-Investigator Team, 2004. HRSC: The High
1166 Resolution Stereo Camera of Mars Express. In: Wilson, A. (Ed.), Mars Express: The
1167 Scientific Payload. ESA SP-1240, Noordwijk, Netherlands: ESA Publications Division, pp.
1168 17–36. ISBN 92-9092-556-6.

1169 Oberbeck VR, Quaide WL. 1967. Estimated thickness of a fragmental surface layer of Oceanus
1170 Procellarum. *J. Geophys. Res.* 72, 4697–4704.

1171 Oberbeck VR, Quaide WL. 1968. Genetic implications of lunar regolith thickness variations.
1172 *Icarus* 9, 446–465.

1173 Pan, L. et al, 2020. Crust stratigraphy and heterogeneities of the first kilometers at the
1174 dichotomy boundary in western Elysium planitia and implications for InSight lander. *Icarus*
1175 338. 113511, doi:10.1016/j.icarus.2019.113511.

1176 Parker, T. J. et al., 2019. Localization of the InSight lander. 50th Lunar and Planetary Science,
1177 Abstract #1948.

1178 Perrin, C., S. Rodriguez, S., Jacob, A., Lucas, A. Spiga, N. Murdoch, R. Lorenz, I. Daubar, L.
1179 Pan, L., T. Kawamura, P. Lognonné, D. Banfield, M. Banks, R. F. Garcia, C. E. Newman,
1180 L. Ohja, R. Widmer-Schmidrig, A.S. McEwen, W. B. Banerdt 2020. Monitoring of Dust-
1181 Devil Tracks Around the InSight Landing Site, Mars, and Comparison with in-situ
1182 Atmospheric Data. GRL accepted in special issue.

1183 Perrin, C., S. Rodriguez, A. Jacob, T. Kawamura, A. Lucas, B. Kenda, A. Spiga, N. Murdoch,
1184 R. F. Garcia, R. D Lorenz, I. Daubar, P. H. Lognonné, D. J Banfield, L. Ohja, M. Banks, L.
1185 Pan and V. Ansan, 2019. Dust devils' signature around the InSight landing site (Mars):
1186 analysis of HiRISE satellite images and SEIS seismic data. AGU, San Francisco, USA.

1187 Presley, M.A., P.R. Christensen, 1997. Thermal conductivity measurements of particulate
1188 materials, Part I: A review. *J. Geophys. Res.* 102, 6535–6549.

1189 Pike, W.T., Staufer, U., Hecht, M.H., Goetz, W., Parrat, D., Sykulska-Lawrence, H., Vijendran,
1190 S., Madsen, M.B., 2011. Quantification of the dry history of the Martian soil inferred from
1191 in situ microscopy. *Geophys. Res. Lett.* 38, L24201, doi:10.1029/2011GL049896.

1192 Piqueux, S., P.R. Christensen, 2011. Temperature-dependent thermal inertia of homogeneous
1193 Martian regolith. *J. Geophys. Res.* 116, E07004. doi:10.1029/2011je003805.

1194 Poulet, F., Bibring, J. P., Langevin, Y., Mustard, J. F., Mangold, N., Vincendon, M., et al.,
1195 2009. Quantitative compositional analysis of martian mafic regions using the MEx/OMEGA
1196 reflectance data 1. Methodology, uncertainties and examples of application. *Icarus*, 201, 1,
1197 69–83, doi:10.1016/j.icarus.2008.12.025.

1198 Rogers, A. D., Bandfield, J. L., 2009. Mineralogical characterization of Mars Science
1199 Laboratory candidate landing sites from THEMIS and TES data. *Icarus*, 203(2), 437–453.,
1200 doi: 10.1016/j.icarus.2009.04.020.

1201 Rampe, E. B., et al., 2018. Sand mineralogy within the Bagnold Dunes, Gale crater, as observed
1202 in situ and from orbit. *GRL* 5, 9488–9497, doi:10.1029/ 2018GL079073.

1203 Reiss D. and Lorenz R. D., 2016. Dust devil track survey at Elysium Planitia, Mars:
1204 Implications for the InSight landing sites. *Icarus* 266, 315-330.

1205 Reiss, D., L. Fenton, L. Neakrase, M. Zimmerman, T. Statella, P. Whelley, M. Balme, 2016.
1206 Dust Devil Tracks. *Space Sci. Rev.* 203 (1-4), 143-181, doi: 10.1007/s11214-016-0308-6.

1207 Rodriguez, S., Perrin, C., Jacob, A., Lucas, A., Kenda, B., Spiga, A., Murdoch, N., Garcia, R.,
1208 Lorenz, R., Daubar, I. J., Lognonné, P., L. Ohja, M. E. Banks, V. Ansan, 2019. Searching
1209 for geological surface changes around the InSight landing site (Mars) from HiRISE satellite
1210 images. EGU, Vienne, Austria.

1211 Ruff, S.W., Christensen, P.R., 2002. Bright and dark regions on Mars: Particle size and
1212 mineralogical characteristics based on Thermal Emission Spectrometer data. *J. Geophys.*
1213 *Res. Planets* 107 (E12), 5127,doi:10.1029/2001JE001580.

1214 Savijärvi, H., T. H. McConnochie, A-M. Harrib, M. Paton, 2019. Annual and diurnal water
1215 vapor cycles at Curiosity from observations and column modeling. *Icarus*, 319, 485-490,
1216 doi: 10.1016/j.icarus.2018.10.008.

1217 Schultz, A. R., 2000. Localization of bedding plane slip and backthrust faults above blind thrust
1218 faults: Keys to wrinkle ridge structure. *J. Geophys. Res.* 105, E5, 12,035-12,052.

1219 Short, N. M, Foreman, M. L., 1972. Thickness of impact crater ejecta on the lunar surface. *Mod.*
1220 *Geol.* 3,69–91.

1221 Smrekar, S.E., Lognonné, P., Spohn, T. et al., 2019. Pre-mission InSights on the Interior of
1222 Mars. *Space Sci Rev.* 215, 3, doi : 10.1007/s11214-018-0563-9.

1223 Smith, D.E. et al., 1999. The global topography of Mars and Implications for surface evolution.
1224 *Science* 284, 1495–1503.

1225 Smith, D.E. et al., 2001. Mars Orbiter Laser Altimeter: experiment summary after first year of
1226 global mapping of Mars. *J. Geophys. Res.* 106, E10, 23698–23722.

1227 Spiga, A., Banfield, D., Teanby, N. et al., 2018. Atmospheric Science with InSight. *Space Sci.*
1228 *Rev.* 214, 7, 1-64, doi:10.1007/s11214-018-0543-0.

1229 Spohn, T. et al., 2018. The Heat Flow and Physical Properties Package (HP³) for the InSight
1230 Mission. *Space Sci .Rev.* 214, 96, doi: 10.1007/s11214-018-0531-4.Squyres, S.W.,
1231 Grotzinger, J.P., Arvidson, R.E. et al., 2004. In situ evidence for an ancient aqueous
1232 environment at Meridiani Planum, Mars. *Science* 306:1709–1714.

1233 Stenonis, N., 1669. *De solido intra solidum naturaliter contento dissertationis prodromus.*
1234 *Florentiae : ex typographia sub signo stellae*, 83 pp.Strom, R.G., 1972. Lunar mare ridges,
1235 rings and volcanic ring complexes. *Mod. Geol.* 2, 133–157.

1236 Suppe J, and W.. Narr, 1989. Fault-related folding on Earth with application to wrinkle ridges
1237 on Mars and the Moon. In MEVTV workshop on tectonics features on Mars, ed. Watters
1238 T.R. and Golombek M.P., LPI Tech. Rep. 89-06, 29-30. Houston, Tex.

1239 Sweeney, J., Warner, N. H., Ganti, V., Golombek, M. P., Lamb, M. P., Fergason, R., Kirk, R.,
1240 2018. Degradation of 100- m-scale rocky ejecta craters at the InSight landing site on Mars
1241 and implications for surface processes and erosion rates in the Hesperian and Amazonian. *J.*
1242 *Geophys. Res. Planets*, 123, 2732–2759, doi: 10.1029/ 2018JE005618.

1243 Tanaka K. et al., 2014. Geologic map of Mars. U.S. Geol. Surv. Sci. Invest. Map 3292.

1244 Tirsch, D., Jaumann, R., Pacifici, A., Poulet, F., 2011. Dark aeolian sediments in Martian
1245 craters: Composition and sources. *J. Geophys. Res.: Planets* 116, E03002,
1246 doi:10.1029/2009JE003562.

1247 Trebi-Ollennu, A., Kim, W., Ali, K. et al., 2018. InSight Mars Lander Robotics Instrument
1248 Deployment System. *Space Sci. Rev.* 214, 93, doi:10.1007/s11214-018-0520-7.

1249 Vaucher, J., et al., 2009. The volcanic history of Central Elysium Planitia: Implications for
1250 martian magmatism. *Icarus* 201, 39-51, doi:10.1016/j.icarus.2009.06.032.

1251 Vincendon, M., C. Pilorget, B. Gondet, S. Murchie, and J.-P. Bibring, 2011. New near-IR
1252 observations of mesospheric CO₂ and H₂O clouds on Mars, *J. Geophys. Res.*, 116, E00J02,
1253 doi:10.1029/2011JE003827.

1254 Viudez-Moreiras et al., D. (2020). Effects of a Large Dust Event in the near-surface atmosphere
1255 as measured by InSight in Elysium Planitia, Mars. *J. Geophys. Res. Planets*, submitted to
1256 this issue.

1257 Walton, O. R., C. P. De Moor, K. S. Gill, 2007. Effects of gravity on cohesive behavior of fine
1258 powders: implications for processing Lunar regolith. *Granular Matter* 9, 353–363, doi:
1259 10.1007/s10035-006-0029-8.

1260 Wang, A., et al., 2006. Sulfate deposition in subsurface regolith in Gusev crater, Mars, *J.*
1261 *Geophys. Res.*, 111, E02S17, doi:10.1029/2005JE002513

1262 Warner, N. H. et al., 2020. An impact crater origin for the InSight landing site at Homestead
1263 Hollow, Mars: Implications for near surface stratigraphy, surface Processes, and erosion
1264 rates. *J. Geophys. Res.*, doi: 10.1029/2019JE006333.

1265 Warner, N. H. et al., 2019. Geomorphology and origin of Homestead hollow, the landing
1266 location of the InSight lander on Mars: LPSC L, abstract 1184, LPI, Houston, TX.

1267 Warner, N. H., M. P. Golombek, J. Sweeney, R. L. Fergason, R. L. Kirk, and C. Schwartz,
1268 2017. Near surface stratigraphy and regolith production in southwestern Elysium Planitia,
1269 Mars: Implications for Hesperian-Amazonian terrains and the InSight lander mission. *Space*
1270 *Sci. Rev.* 211, 147–190, doi:10.1007/s11214-017-0352-x.

1271 Watters, T. R., 1988. Wrinkle Ridge Assemblages on the Terrestrial Planets. *J. Geophys. Res.*
1272 93, b9, 10,236-10,254.

1273 Watters, W. A., Geiger, L. M., Fendrock, M. A., Gibson, R., 2015. Morphometry of small recent
1274 impact craters on Mars: Size and terrain dependence, short-term modification. *J. Geophys.*
1275 *Res. Planets*, 120, 226–254, doi:10.1002/2014JE004630.

1276 Weitz, C. M., J. A. Grant, N. H. Warner, M. P. Golombek, S. A. Wilson, E. Hauber, V. Ansan,
1277 C. Charalambous, N. Williams, F. Calef, T. Pike, H. Lethcoe, J. Maki, A. DeMott, and M.
1278 Kopp, 2019. Clast sizes and shapes at the InSight landing site, 2019. 50th LPSC #1392,
1279 Houston, USA.

1280 Wentworth, C. K., 1933. Fundamental limits to the sizes of clastic grains. *Science* 77, 633-634,
1281 doi: 10.1126/science.77.2009.633.

1282 Werner, S. C., 2009. The global Martian volcanic evolutionary history. *Icarus* 201, 44– 68,
1283 doi:10.1016/j.icarus.2008.12.019.

1284 Williams, N. R. et al., 2019. Surface alteration from landing InSight on Mars and its implications
1285 for shallow regolith structure. 50th LPSC, Houston, USA.

1286 Wilson, S., N. H. Warner, J. A. Grant, M. Golombek, C. M. Weitz, A. DeMott, M. Kopp, E.
1287 Hauber, V. Ansan, C. Charalambous, W. T. Pike, H. Lethcoe-Wilson and R. Hausmann,
1288 2019. Crater Retention Ages at the InSight and Spirit Landing Sites. AGU, San Francisco,
1289 USA.

1290 Wippermann, T., T.L. Hudson, T. Spohn, L. Witte, M. Scharringhausen, G. Tsakyridis, M.
1291 Fittock, O. Krömer, S. Hense, M. Grott, J. Knollenberg, R. Lichtenheldt, 2020. Penetration
1292 and performance testing of the HP³ Mole for the InSight Mars mission. Planetary and Space
1293 Science 181, 104780.

1294 Yen, A. S., et al. (2008), Hydrothermal processes at Gusev Crater: An evaluation of Paso Robles
1295 class soils, J. Geophys. Res., 113, E06S10, doi:10.1029/2007JE002978.

1296 Yingst, R. A., et al. (2013), Characteristics of pebble- and cobble-sized clasts along the
1297 Curiosity rover traverse from Bradbury Landing to Rocknest, J. Geophys. Res. Planets, 118,
1298 2361–2380, doi:10.1002/2013JE004435.

1299 Zimbelman, J. R., 2010. Transverse Aeolian Ridges on Mars: First results from HiRISE images,
1300 Geomorphology, 121, 22–29, doi:10.1016/j.geomorph.2009.05.012.

1301 Zimbelman, J. R., L. J. Griffin, 2010. HiRISE images of yardangs and sinuous ridges in the
1302 lower member of the Medusae Fossae Formation, Mars. Icarus 205, 198-210,
1303 doi:10.1016/j.icarus.2009.04.003.

1304

1305 Tables:

1306 Table 1. Morphometric laws for Martian impact craters. D: diameter, d: depth and h:
1307 crater rim. See figure 1d for sketch.

Author	D	d	h	unit
Garvin (2003)	$3 \text{ km} \leq D < 7 \text{ km}$	$0.21 * D^{0.81}$	$0.04 * D^{0.31}$	h and D in km
Garvin (2003)	$7 \text{ km} \leq D < 100 \text{ km}$	$0.36 * D^{0.49}$	$0.02 * D^{0.84}$	h and D in km
Watters et al., 2014	$50 \text{ m} \leq D < 2 \text{ km}$	$0.223 * D^{1.012}$	$0.0354 * D^{1.017}$	h and D in km
Sweeney et al., 2018	$10 \text{ m} < D < 1.2 \text{ km}$	$0.081 * D$	$0.029 * D$	h and D in m

1308

1309 Table 2. Minimum lava thickness T calculated from MOLA data. Crater diameter D is
1310 measured, depth d and rim height h are calculated, using Garvin's (2003) equations for fresh
1311 crater (see Table 1). Lava thickness is then deduced for buried (B) impact craters and estimated
1312 for partly buried (PB) craters, using the relief between the Garvin's rim height (h) and the
1313 remnant rim height (hr). See the text for explanation.

Labeled crater	Type	Diameter D (m)	Depth d (m)	Rim height h (m)	Plain	Max rim	Rim height hr (m)	Lava thick. T (m)
					elevation	elevation		
					h_{plain} (m)	hr_max (m)		
		MOLA	Garvin	Garvin	MOLA	MOLA	MOLA	MOLA
c1	PB	4150	665	62	-2700	-2681	19	43
c2	B	14240	1323	186				186
c3	B	3070	521	57				57
c4	PB	4860	756	65	-2635	-2594	24	41
c5	B	3022	514	56				56
c6	PB	8894	1050	125	-2600	-2430	170	-45

1314

1315

Figures :

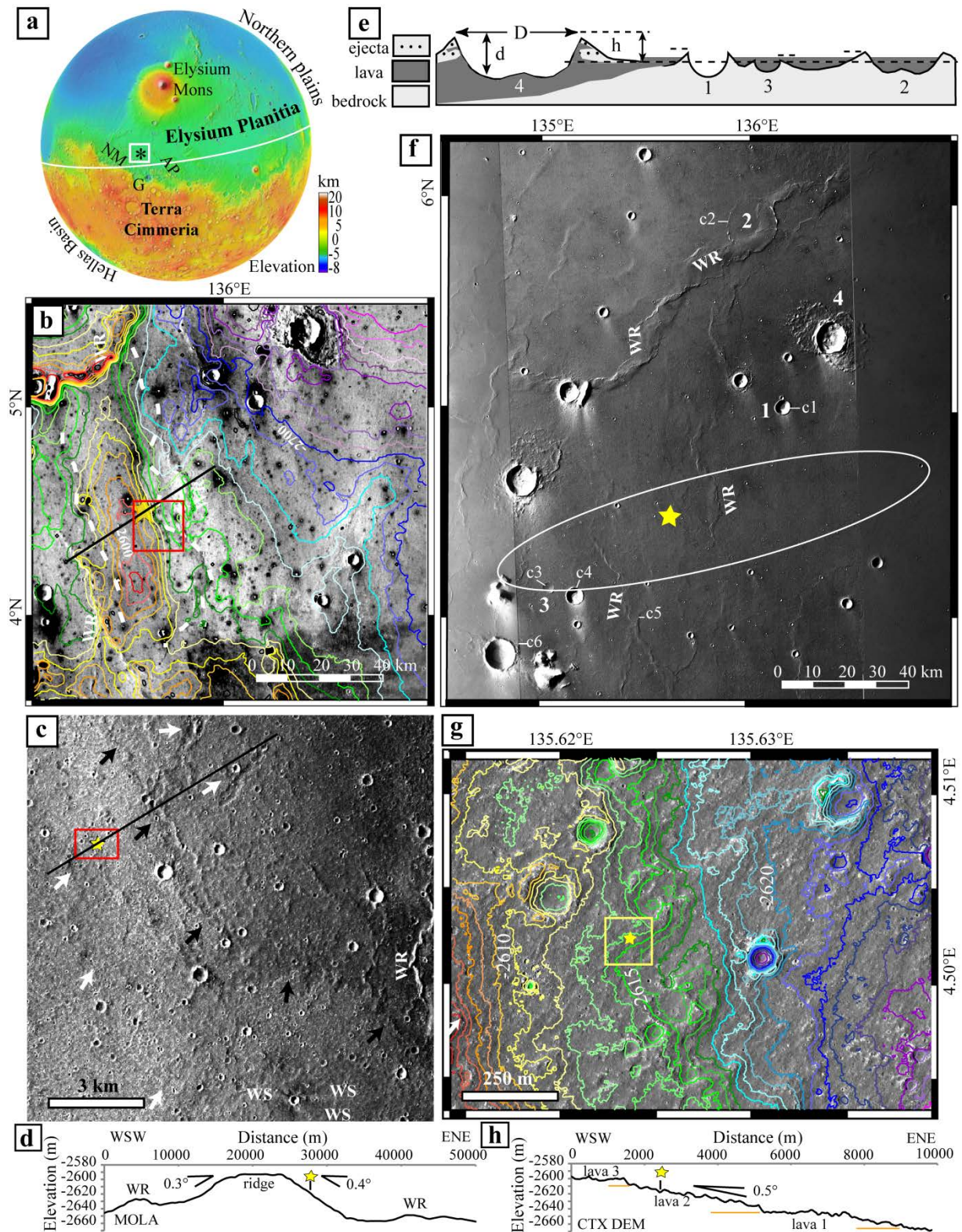


Figure 1: a. InSight landing site (*) located on MOLA topography at elevation of -2600m in the western Elysium Planitia, near the equator between northern plains and Elysium Mons, and the southern highly cratered highlands, Terra Cimmeria. AP: Aeolis Planum, G: Gale crater and NM: Nepenthes Mensae. b) Landing area pre-viewed by daytime thermal infrared

THEMIS images at resolution of $100\text{m}\cdot\text{pixel}^{-1}$: Relatively bright plains on which impact ejecta are dark, due to sprayed basaltic materials. Color lines are MOLA elevation contours with a height interval of 10m. White dashed line borders the volcanic ridge. Yellow star is the InSight landing site. c) CTX image close-up (red box in b) showing lobate fronts of three superposed lava flows marked by arrows. WR indicates wrinkle ridges and WS are wind streaks (F04_037262_1841, at resolution of $6\text{m}\cdot\text{pixel}^{-1}$). Red box is location of HiRISE close-up viewed in g. d) WSW-ENE trending MOLA topographic profile across volcanic ridge (see its location in b). e) Sketch of impact crater morphology filled by lava flows, showing different steps (1 to 3) and impact crater postdating the lava deposit (4). Not at scale. D: Impact crater diameter, d: crater depth and h: crater rim. f). Mosaic of HRSC visible nadir images at resolution of $20\text{m}\cdot\text{pixel}^{-1}$ (hc499, hc573, hd628 orbits), on which the planned landing ellipse and landing site are reported. WR is wrinkle ridge. Number corresponds to stage of impact crater filling by lava flows. c# corresponds to crater from which lava thickness was calculated. g) Landing area viewed from visible HiRISE image at resolution of $0.25\text{m}\cdot\text{pixel}^{-1}$: (May, 6, 2014, ESP_036761_1845) on which HiRISE elevation contours of 1m are reported. h) WSW-ENE trending CTX topographic profile across volcanic lava flows (see its location in c). Yellow star shows the location of InSight lander.

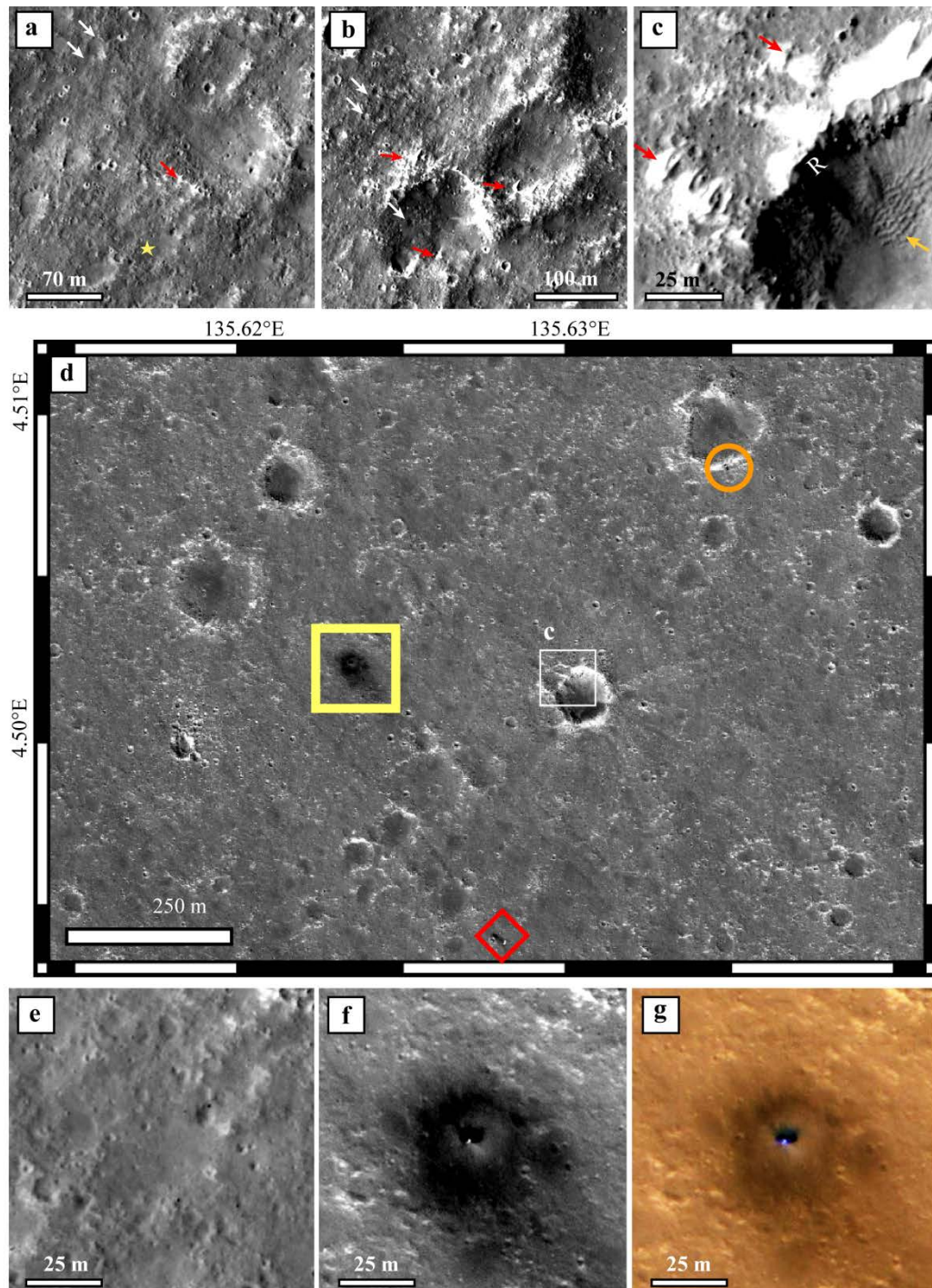


Figure 2: Geological features observed from HiRISE images. a, b, and c correspond to close-ups of the InSight landing site before the landing (May, 6, 2014, ESP_036761_1845). Star shows the InSight location. a) Highly cratered surface on which remain relics of degraded ~100m impact rim and relatively circular hollows smaller than 30 m in diameter. Some of them display smooth inner surface on which NW-SE trending, dark, linear features occurred (white arrows) by wind erosion (dust devil) and small bright linear structures (dunes) can be observed in the orthogonal direction (red arrows) on rim relics. b) Close-up centered on 135.6227°E/4.5128°N showing more preserved degraded impact craters, dust devils tracks and dunes. c) Crescent dunes (red arrows) settled on the NW side of impact crater located at 135.6304°E/4.5013°N. A ripple field is observed inside the crater (orange arrow). R

corresponds to the layered impact rim. d) The landing area viewed December, 6, 2018 (ESP_057939_1845), on which the yellow square indicates the landing site; the orange circle is the location of heat shield, and the red diamond the location of backshell attached to parachute. e, f, and g are the close-up of the landing site viewed by HiRISE camera in 2014, 2018 in visible bands, and in false color (IRB) respectively. Note that the lander marked by a bright spot disturbed dust over a fair distance around it and it has darkened the surface.

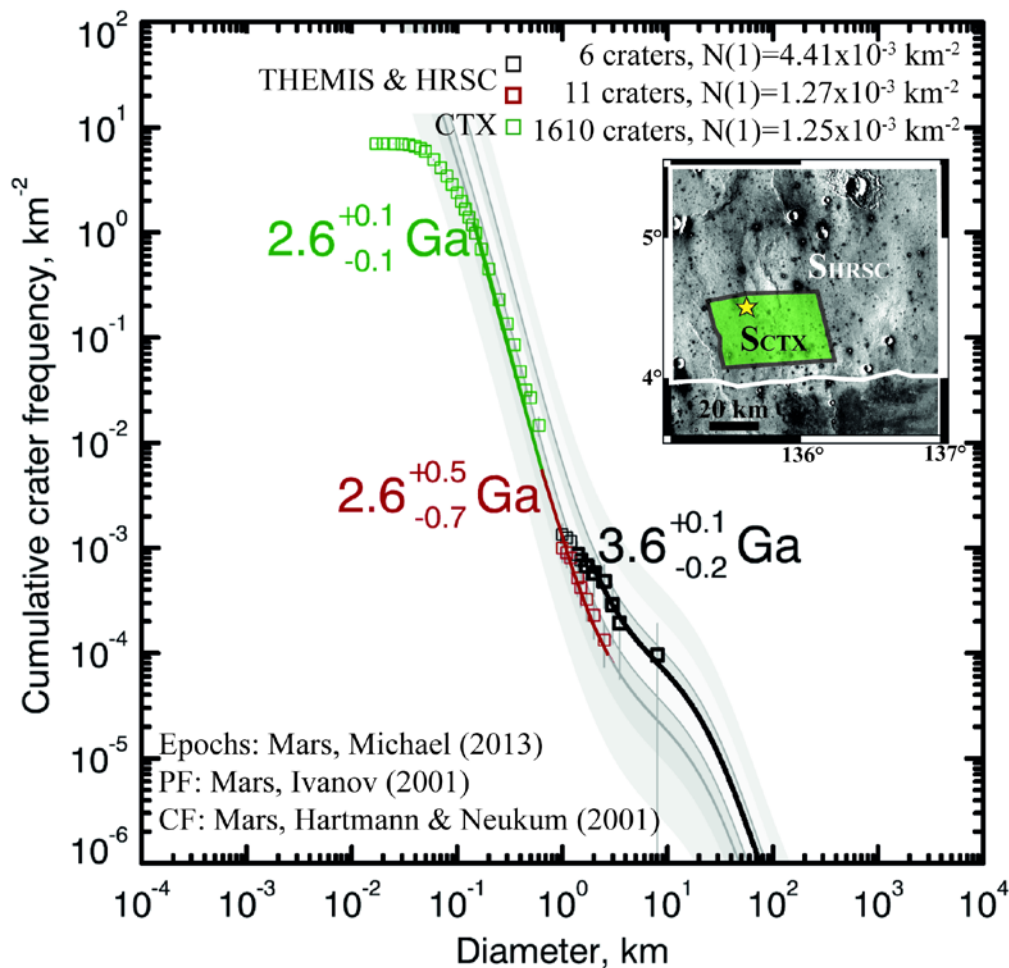


Figure 3: Cumulative crater size-frequency distribution plots for InSight landing site (yellow star). Solid black line: Isochron fitted to diameter bins (2.0-9.0 km) interpreted as containing primarily craters, which have accumulated on the volcanic surface (S_{HRSC} : 10,437.099 km^2 above 3.95°N, based on HRSC and THEMIS data). Solid red line: Isochron fitted to diameter bins (0.7-2.0 km) interpreted as containing primarily craters, which have accumulated after a resurfacing of the volcanic unit from the HRSC and THEMIS data. Solid green line: Isochron fitted to diameter bins (0.15-0.7 km) interpreted as containing primarily craters, which have accumulated on the volcanic surface (S_{CTX} : 1642.369 km^2), based on CTX images.

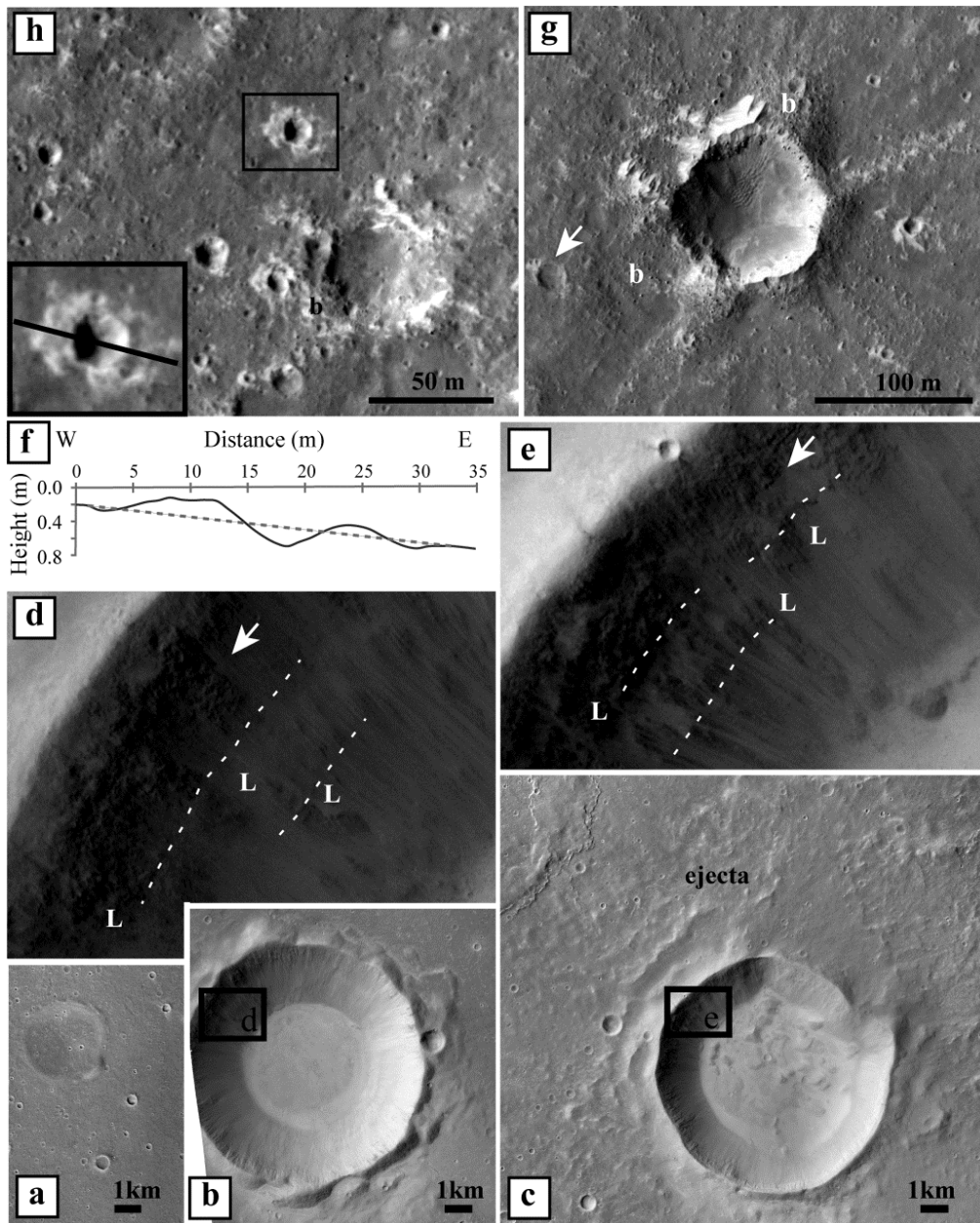


Figure 4: Morphology of impact craters and implication for nature and thickness of geological units. a) Buried impact crater c#3 in figure 1f. b) partly buried ~9 km-in-diameter impact crater c#6 in figure 1e. c) Relatively fresh ~8 km-in-diameter post-dating the last event of Early Amazonian lava flows. d and e) Inner crater sides showing dark layered material (L) up to 500m below the crater rims marked by white arrows. a, b, c, d and e) are extracted from CTX image D18_034071_1842. f) HiRISE topographic profile extracted across a ~11 m relatively fresh impact crater viewed in box of h. g) 100m-in-diameter impact crater showing boulder-rich degraded ejecta corona located 430m east of InSight site (box c Fig. 2d). b: boulders. White arrow shows a 20m impact crater with no boulder around it. h) Morphologies of impact craters in function of their diameter on the smooth surface of landing area. Note that the 50m impact crater, located at 190m to the south of InSight site has very few boulders and the smaller ones display no boulder. g and h are extracted from HiRISE image ESP_036761_1845.

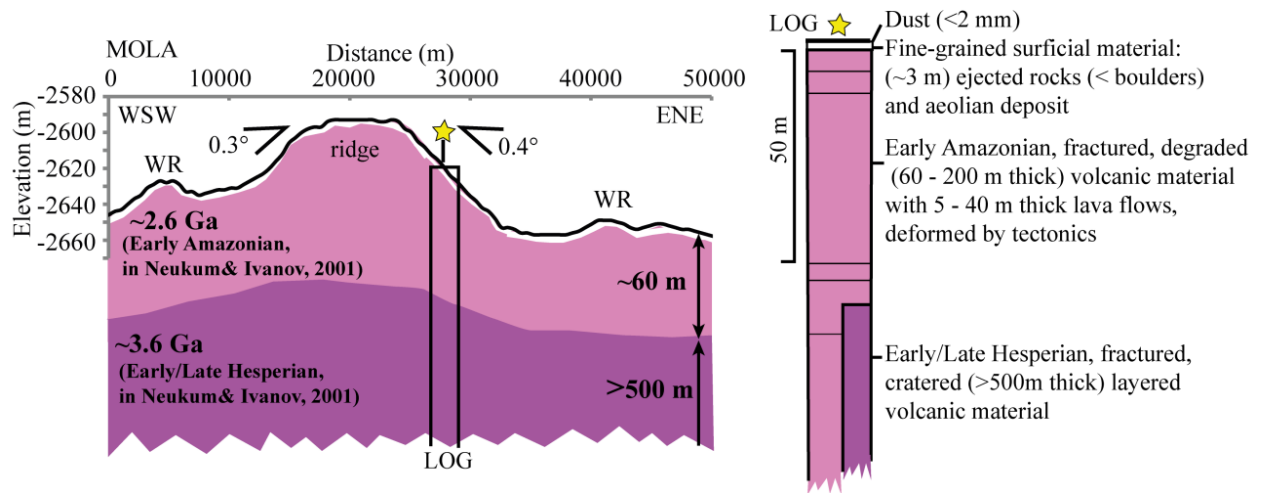


Figure 5: The stratigraphy at the landing site (yellow star) deduced from orbital data. On the left, geologic cross-section based on MOLA topographic profile viewed in Fig. 1c. The vertical scale is exaggerated. On the right, the first 100m thick log. See the text for explanation.

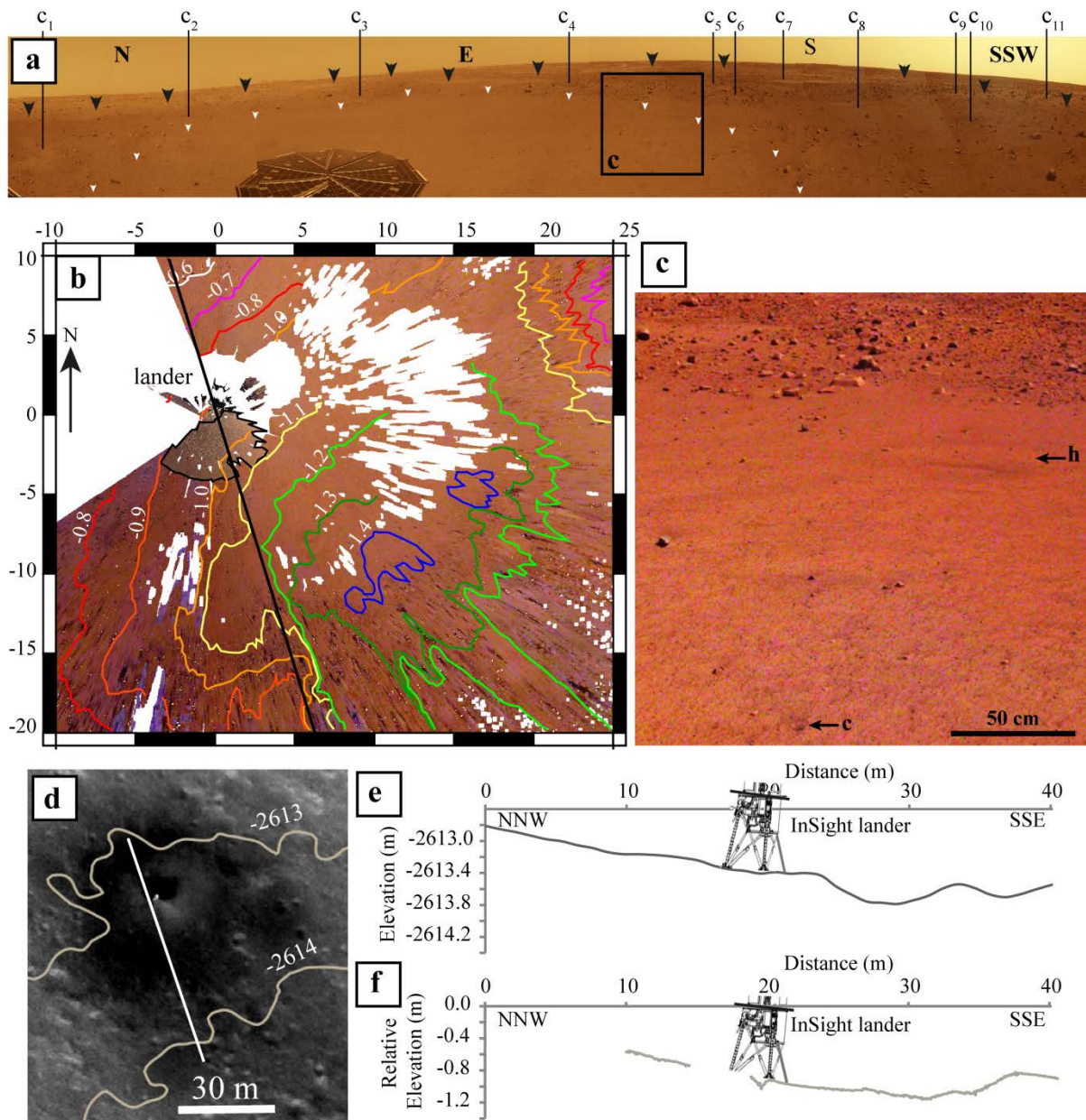


Figure 6: a) InSight sol 14 (December 10, 2018) IDC panorama of the mid-field terrain around the lander from NNW to SSW in clockwise view (D_LRGB_0014_RAS030100CYL_R SCIPANQM1). Black triangles show the outer halo line of dust deposit and white triangles show the inner halo boundary. The $c\#$ symbol indicates the location of impact craters. b) Mosaic of individual IDC images projected in local equirectangular projection centered on the lander (0, 0). The grid unit is meter and North is up. The color lines are local height contours with a height interval of 10 cm with a height origin located at lander desk. White areas are without datum. Black line corresponds to the location of topographic profile viewed in E. Area underlined by black line corresponds to workstation in which SEIS seismometer and HP3 probe will be installed. c) Close-up of panorama, showing 6cm-in-diameter impact crater c and ~meter-in-diameter hollow h probably formed by impact. Note that their rims are without rocks. d) HiRISE image (12/6/2018), on which MOLA elevation contours are reported. White line corresponds to

location of topographic profile viewed in e. e and f) Topographic profiles on which the lander location and attitude are plotted from HiRISE and IDC topography respectively.

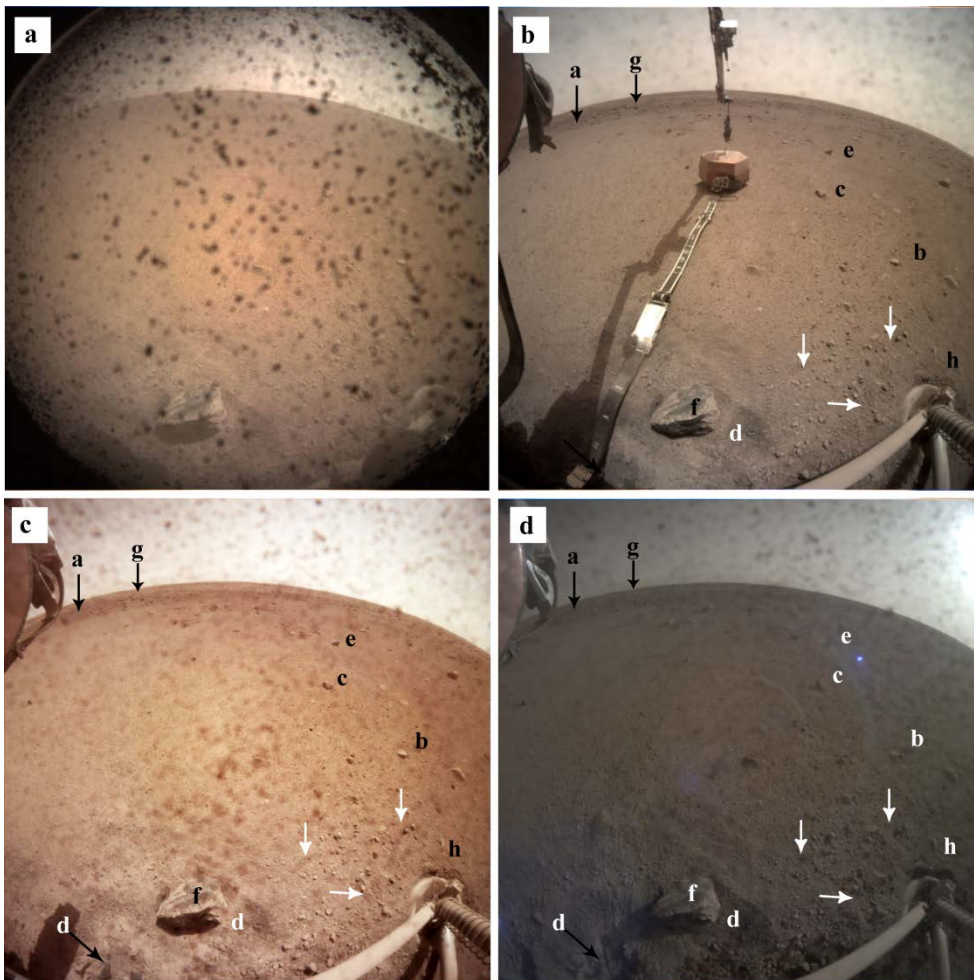


Figure 7: Evolution of the southern area of Homestead hollow (landing site) viewed by the ICC. Each ICC image has a field of view of 124 x 124 degrees. a) The first image (C000M0000_596533559EDR_F0000_0106M8) acquired on November 26, 2018 (Sol 0 of the InSight mission) where the local true solar time for the image exposure was 13h34 PM. b) This image (C000R0063_602124400EDR_F0000_0121M2) was acquired on January 30, 2019, (Sol 63 at 12h48 PM). Note the camera lens is cleaner because the dusty particles were removed by wind. c) ICC image acquired on December 12, 2018 (sol 16) at local true solar time of 13h09 PM (C000M0016_597952811EDR_F0000_0500M2) and d. The same area viewed sol 16 at 16h11 PM (C000M0016_597964044EDR_F0000_0461M2), in which shadows of microstructures are enhanced. At the foreground, the western lander foot (right lower corner) has sunk into a cohesionless material. The hollow surface appears relatively flat with randomly sparse stones. In three images (b, c and d): a. The inner slope of Homestead hollow, ~17 m from the InSight lander; b. Light-toned, flat, pebble; c. and e. Dark-toned, sub-angular pebbles; f. Dark-toned cobble showing a corrugated surface; g. Dark-toned, rounded boulder outside the Homestead hollow; h. Small clod, few cm away from the western lander foot.

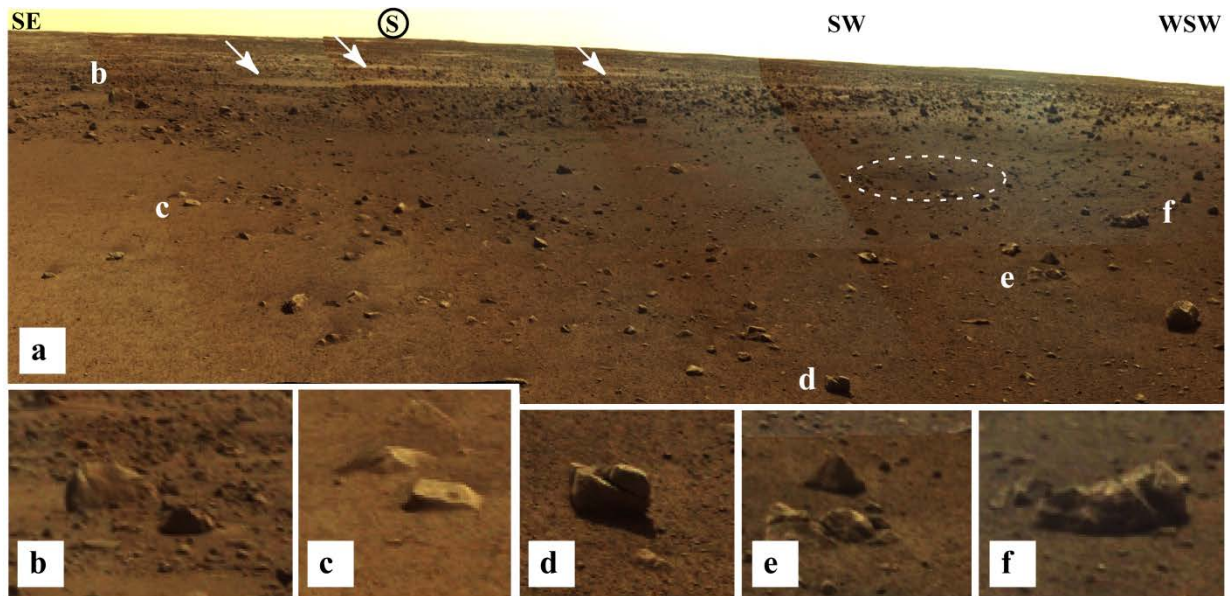


Figure 8: a) Central part of the first panorama acquired sol 14, covering the western Elysium planitia between SE and WSW trends. Notice that the southeastern part of Homestead hollow is brighter and smoother than the southwestern part with coarser clasts (pebbles to cobbles). The south area shows well defined slope of $\sim 3^\circ$ towards the center of hollow whereas the western edge of Homestead hollow shows a slight slope of $\sim 1.5^\circ$ towards the east. In the latter, see the ~ 1.5 m in diameter, shallow depression (dashed white circle) due to meteorite impact, surrounded by a pebble circle. The white arrows show other hollows outside Homestead hollow filled by brighter and probably sandy material. The rocks (b to f) scattered on the surface show different colors, shapes and textures: b. Boulder at the edge of Homestead hollow (~ 1.5 m long, < 1 m high). Note the ventifact, dark-toned, cobble at the front of boulder; c. ~ 10 cm long, ~ 5 cm thick, light-toned, flat top pebbles; d. ~ 10 cm equant, dark-toned pebble showing a sharp oblique fracture; e. Scatter of pebbles with different colors. Note that the dark one is characterized by typical aeolian erosion (ventifact); f. ~ 20 cm long cobble with a heterogeneous texture (several indurated clasts? breccia?).

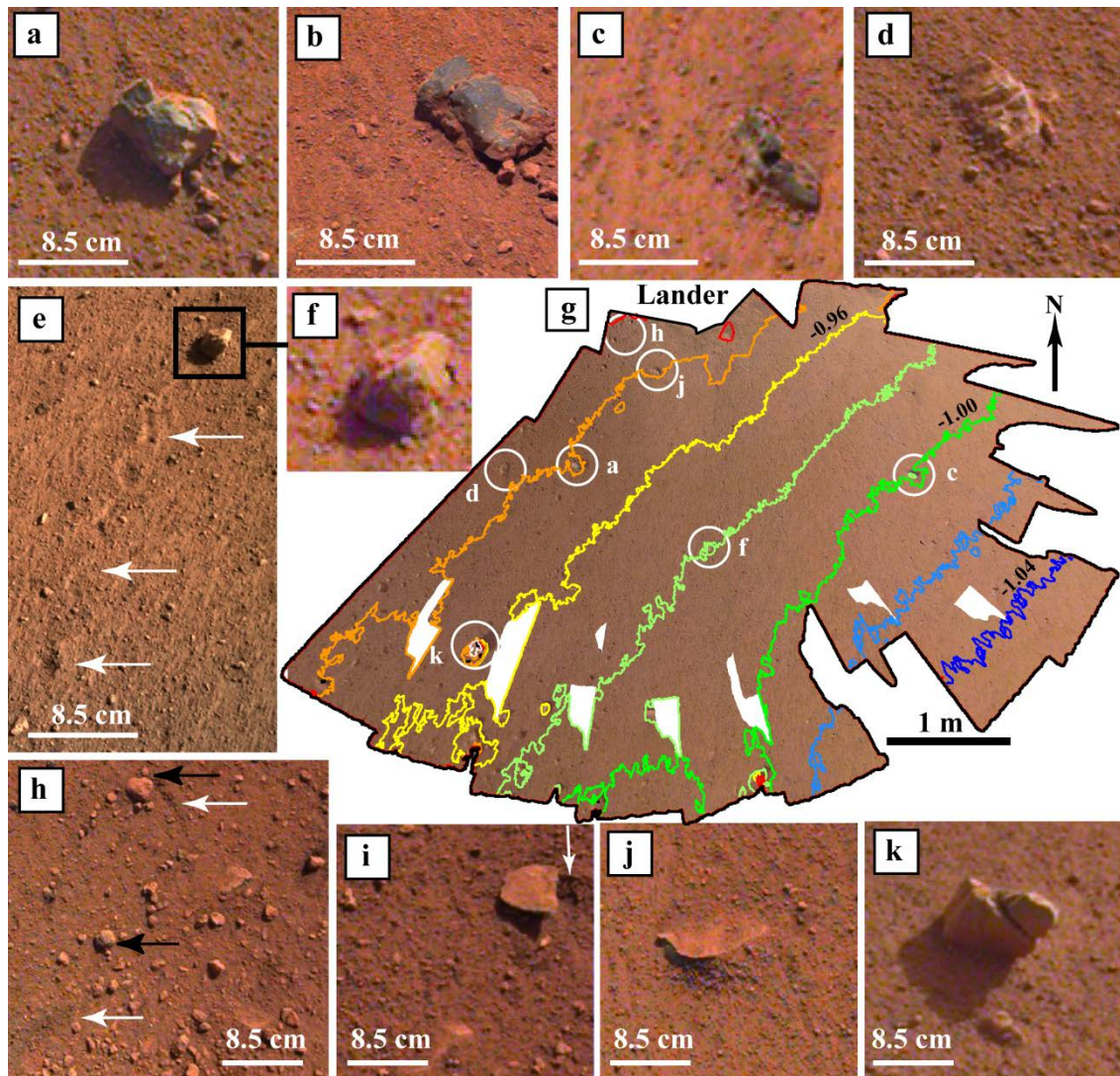


Figure 9. Ejected pebbles and cobbles on the InSight landing workspace: a) 8 cm wide piece of breccia composed of cm-scale angular, dark-toned clasts (D036R0012_597605746CPG_F0101_0060M2) and b) Same cobble viewed from east (D000M0128_607888894CPG_F0000_0846M3). c) partly buried piece of breccia (D000M0076_603267350CPG_F0000_2699M1). d) partly buried piece of breccia composed of light-toned and dark-toned cm clasts (D036R0012_597605746CPG_F0101_0060M2). e) Rolling stone in cohesionless sandy material (D001L0016_597958573EDR_FS0S0SS080M1). White arrows display prod mark (at the foreground) and 52 cm long sinuous roll marks. f) Relatively light-toned, brecciated stone (D000M0070_602751416CPG_F0000_0250M1). g) Equi-rectangularly projected workspace IDC images in front of lander with a spatial resolution of 1 mm. Color lines are relative height contours with an intervals of 2 cm. Labeled circles indicate the location of pebbles. h) Displaced pebbles (black arrows) near the west lander foot with their roll and groove marks (white arrow) in sandy material (D003R0012_597602303CPG_F0101_0060M2). i) Up lifted and few cm pushed away light-toned pebble remaining a trough mark (white arrow) (D003R0012_597602303CPG_F0101_0060M2). j) partly buried, light-toned pebble with saddle sharp crestline (D003R0012_597602303CPG_F0101_0060M2). k) Dark-toned, sub-angular pebble showing oblique planar fracture (D016R0014_597779204CPG_F0103_0100M1). All images are oriented North up.

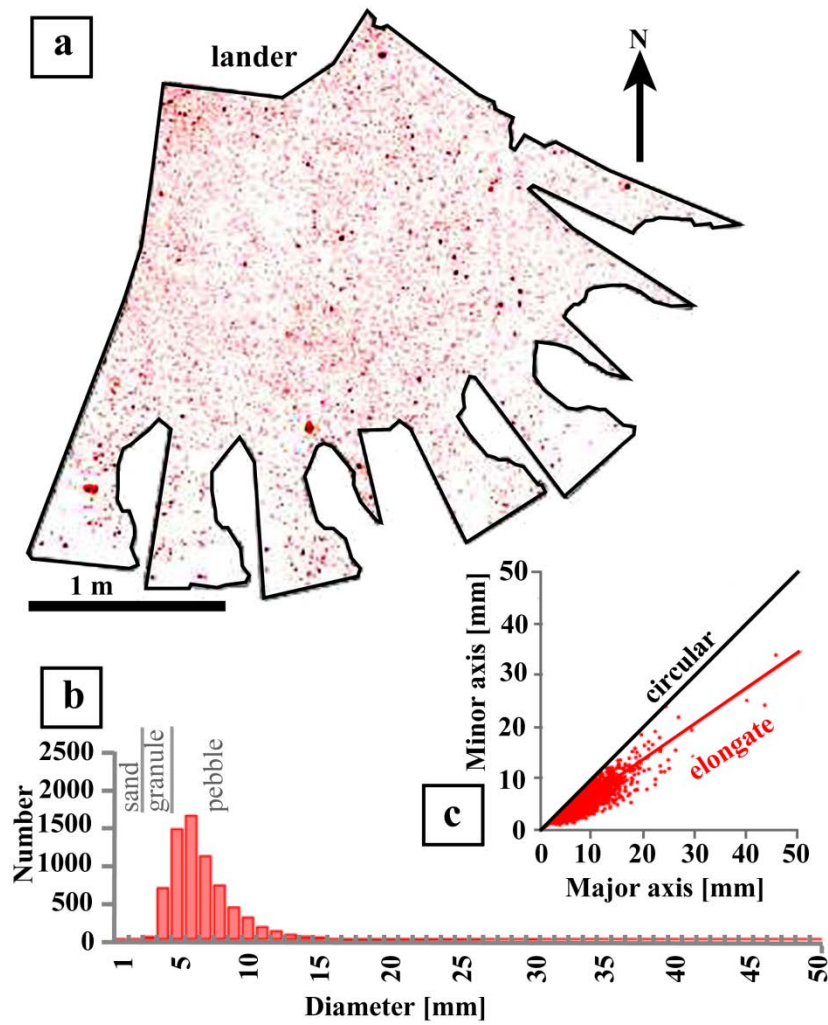


Figure 10. a) Clast distribution into workspace ($N=8252$; area 5.339m^2). b) Particles sizes over the measured diameter range (range=2 mm to 50 mm; mean=5.96 mm) on which modified Wentworth classes are superimposed (sand, granule and pebble). c) Diagram showing 2D clast shape (equant to sub-equant).

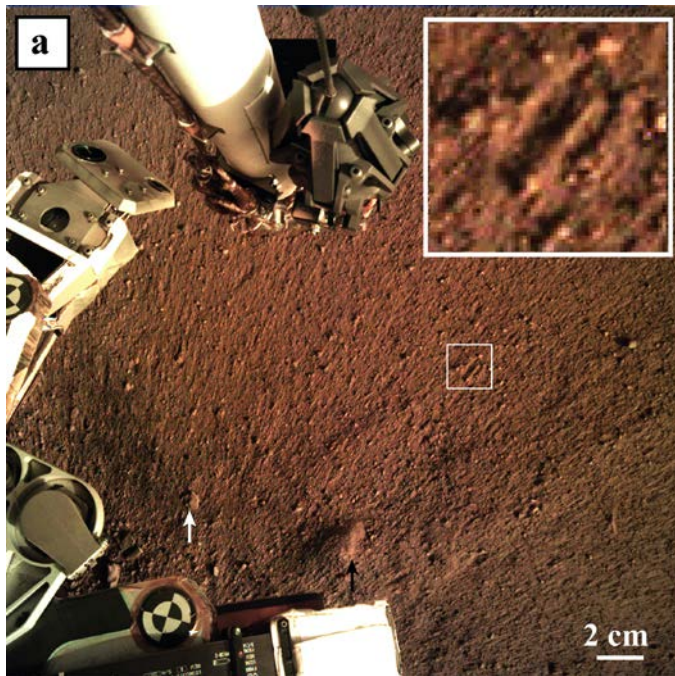


Figure 11. Sandy surface near lander in workspace. a). The Instrument Deployment Camera acquired this image (D000M0008_597253045EDR_F0000_0463M1) on December 5, 2018 (Sol 8) when the local true solar time was 16h01. The ground surface is striated and scoured, with multi-millimeter relief ridges and troughs that extend radially away from the lander. Some granules and small pebbles have tails extending away from the lander (see insert), suggesting that material behind small clasts has been preserved from erosive rocket blast. Note partly buried sub-rounded pebble (black arrow) and angular, very flat pebble (white arrow) on the darker ground near the lander.

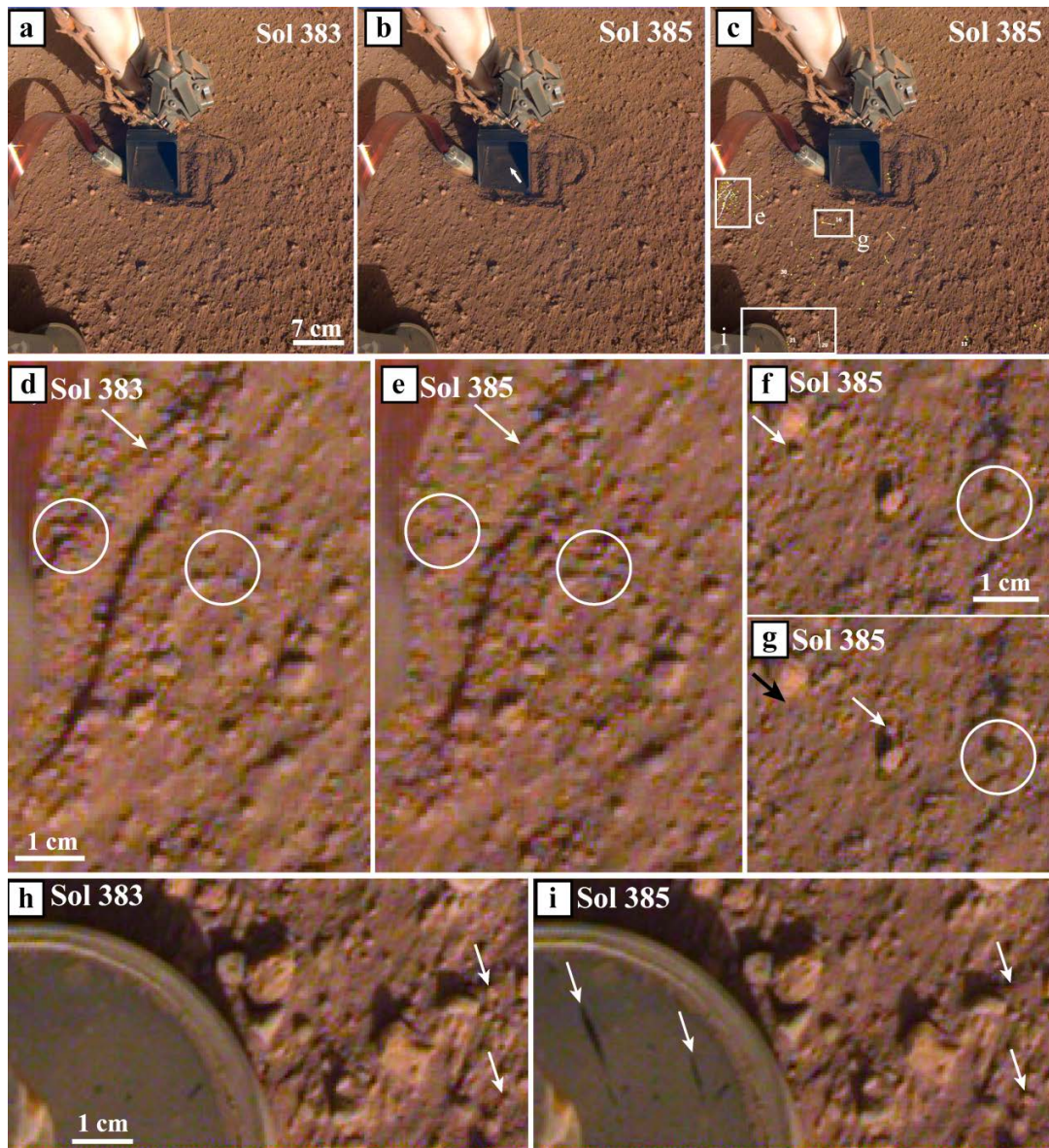


Figure 12. Aeolian changes on the Martian ground surface near HP3 mole. All images are oriented with the North down. a) IDC image acquired sol 383 at 16h around (D000M0383_630540698CPG_F0000_0250M1). b) IDC image acquired sol 385 at the same time (D000M0385_630718248CPG_F0000_0250M1). c) Location of Aeolian changes (yellow point is the starting location and green point the ending one). No plot into the scoop, although coarse grain displacement has been observed and very fine particles have been added between the two snapshots (white arrow in b). d and e) Close-ups in the western side of observed area: Notice that the mass-wasting of scour sides occurred (white circle), leading to partial removal and new arrangement of clastic material transported by creeping towards NE trending as imprinted by faint striation into the ground. It is not possible to determine the diameter of individual transported particles. The size of clastic patch or moat is around mm scale. f and g) Displacement of coarse sand/granule grain (2.5 ± 0.7 mm) of around 2 cm, marked by black and white arrow. This grain could be a candidate for saltation process because no striation path appears on the ground. Notice that the cleaning of coating pebble occurred during this aeolian event (white circle). h and g) Potential displacement of sand grain by saltation around 2 cm (white arrows on the ground). Note the black elliptical features on the surface of HP3 foot that are oriented parallel to the measured wind direction, suggested that small particles impinges the surface like a “splash”.

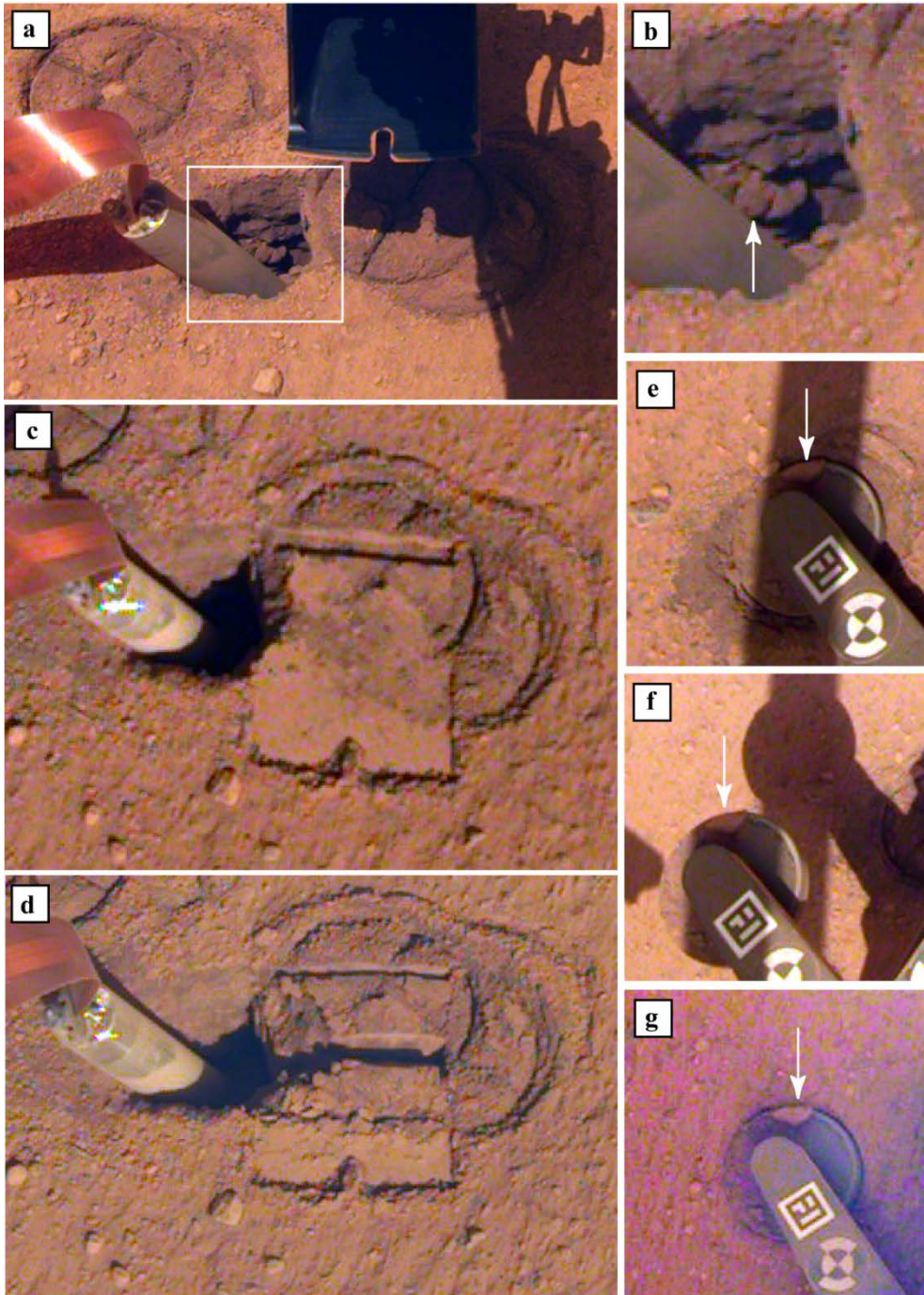


Figure 13. Ground texture near HP3. a). IDC image acquired (D000M0235_617388344CPG_F0000_0250M1, sol 235) b) . Close-up of few centimeter deep cross-section at HP3 mole hole shows a fine layered material composed of very fine sand, granules, small pebbles and aggregates of small pebbles (white arrows). Notice that the ground is darker than the red clastic lamina at the surface. c) IDC image acquired (D001L0243_618107964CPG_F0101_0028M3, sol 243) after the first scoop push. d) IDC image acquired (D003L0250_618729516CPG_F0101_0028M2, sol 250) after the test scoop. e) HP3 left rear foot with a sample of indurated fine sand (white arrow). f) During HP3 lift, the sample remains at the same place although the foot is tilted. (D000M0203_614553629CPG_F0000_0824M1) G. After three lifts, the sample of indurated fine sand keeps its location on the foot. (D000M0209_615090548CPG_F0000_0817M1, sol 209).

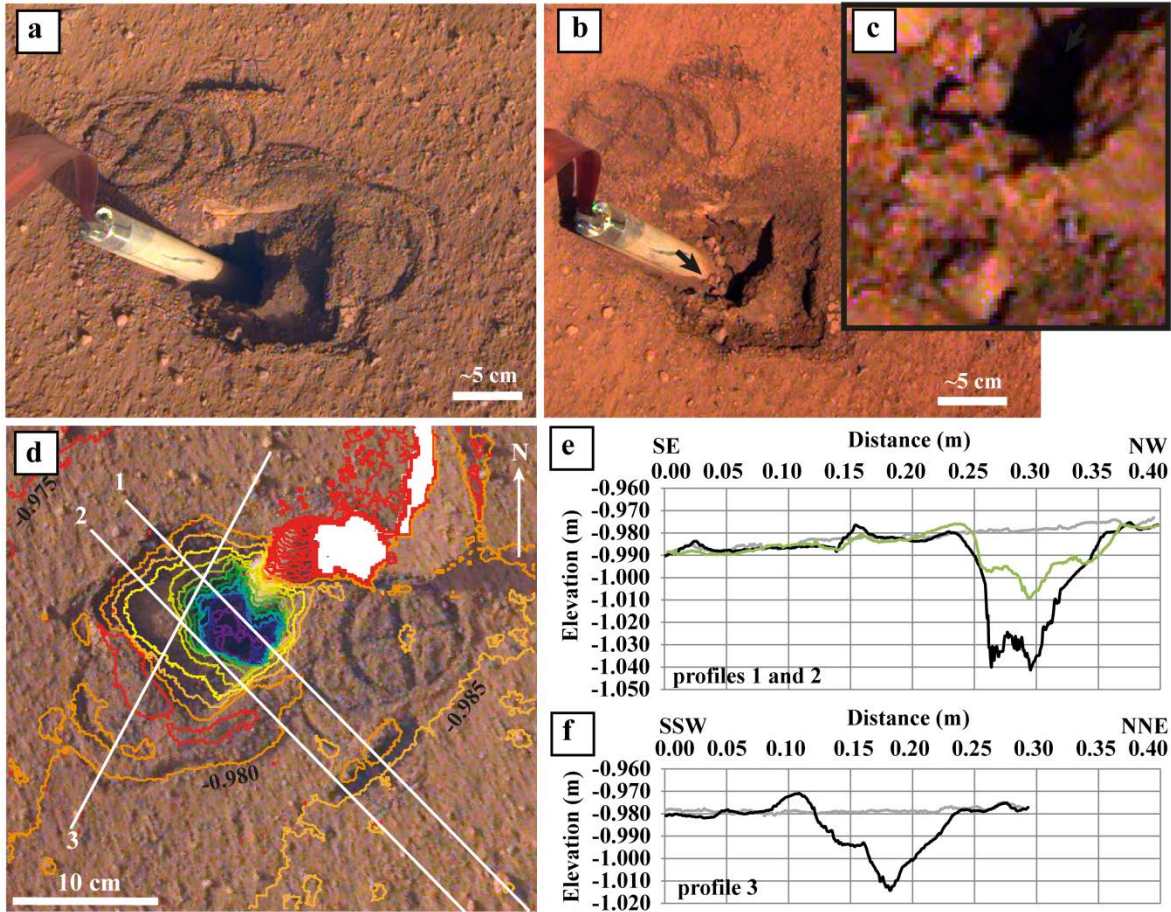


Figure 14. Sub-surface near HP3 after scoop scraping and pushing tests. a) IDC image acquired sol 417 at 16h10 (D000M0417_633558206CPG_F0000_0473M1). b) The same area viewed three days after IDC image acquired sol 421 at 13h54 (D000M0421_633904709CPG_F000_0250M1). c) Close-up of the hole showing pebbles down the hole. Location indicated by black arrow in b. For previous images, north is down. d) Ortho-rectified image and DEM acquired sol 417. Color lines are height contours at intervals of 5 mm. White areas have no data. e and f) Topographic profiles across the hole with relative distance. Gray ones correspond to pristine profiles acquired sol 14. Dark one corresponds to topographic profiles 1 and 3. Green one is profile 2 on Fig. 14d.

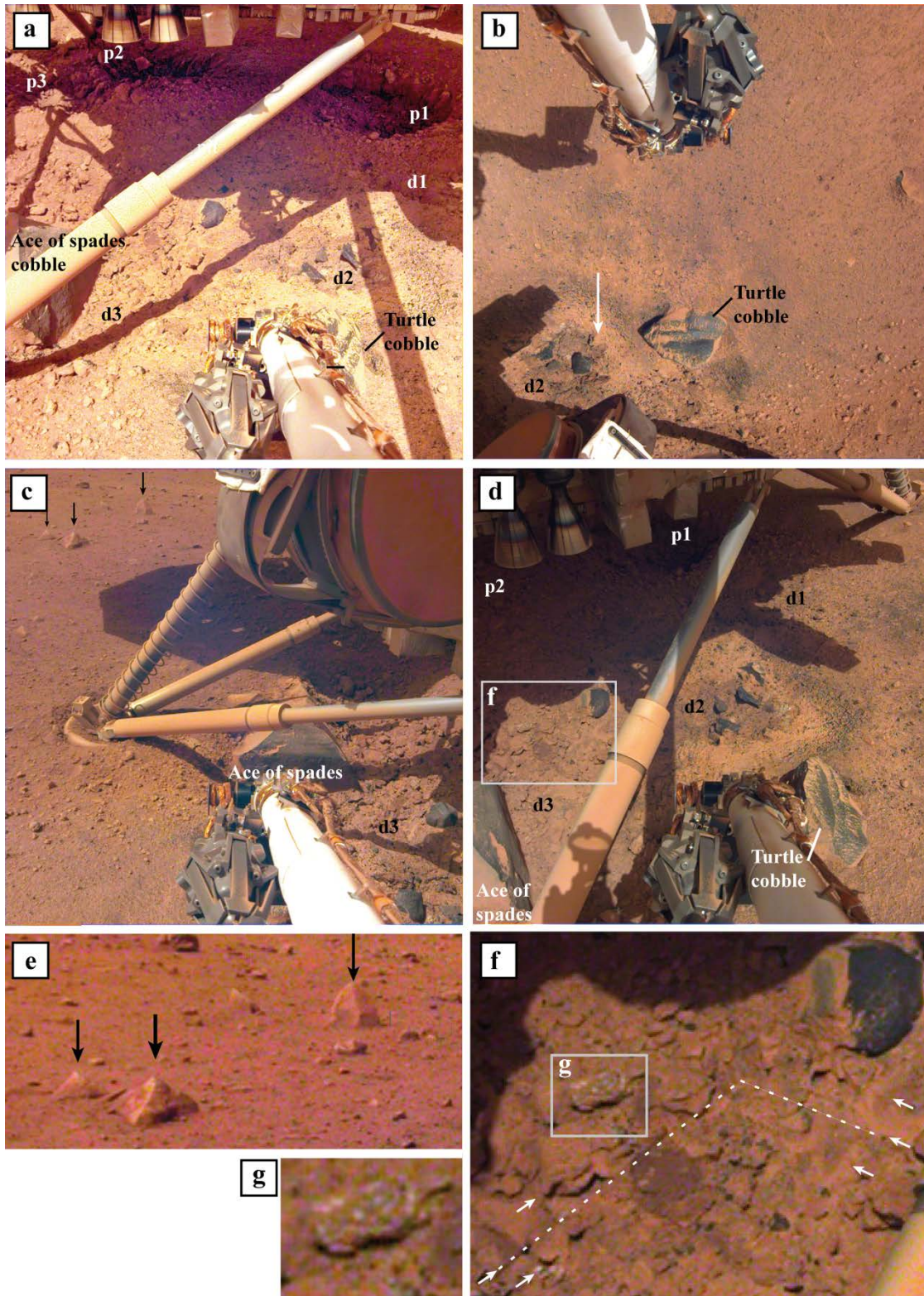


Figure 15. Geologic surface beneath the lander. a) IDC image (D001R0018_598131636CPG_F0606_0010M1), acquired sol 18 at 13h29, shows terrain disturbed by retro-rockets (seen at the top of image) under the lander: shallow depressions (d#) composed of poorly sorted, dark-toned, angular gravels and pebbles at the forefront, and pits (p#) bordered by a cm-scale deep, steep slope (greater than the angle of repose) clastic material in the background. Two cobbles are present near the western lander foot (Ace of Spades) and in front of lander (Turtle). b) IDC image (D001L0014_597774194CPG_F0909_0010M1, sol 14 at 12h52) shows few cm-deep left pit

which steep edges are irregular, composed of few mm thick, indurated, light-toned, fine-grained material (white arrow), and partly cementing cm-scale clasts locally, and covering a clastic material composed of dark-toned, angular to sub-rounded pebbles poorly sorted in a very fine grained material. c) IDC image (D001R0018_598130890CPG_F0707_0010M1, sol 18 at 13h17), shows evidence for slight sliding and digging of the western footpad into place, creating a depression on one side and clods of material in left side, suggesting the sub-surface consists of surficial dust mixed with thin, cohesionless, fine-grained material. Black arrows show three pyramidal stones sculpted by wind (ventifacts). d) IDC image (D002R0018_598131254CPG_F0707_0010M1, sol 18 at 13h22) shows the front side of lander and the eastern footpad completely sunk in ground. Behind the Turtle cobble, the small pit shows a diversity of materials. e) Zoom on ventifacts seen in C, showing that their base was preserved of wind action before the removal of fine-grained material. The thickness of removal material is estimated to some centimeters. f) Close-up of pebbles beneath the lander showing a variety of sizes and lithologies (see text). Tenuous plane beddings are observed (white arrows and lines). g) Close-up of pebble composed of mm-scale, coarse, light-toned minerals.

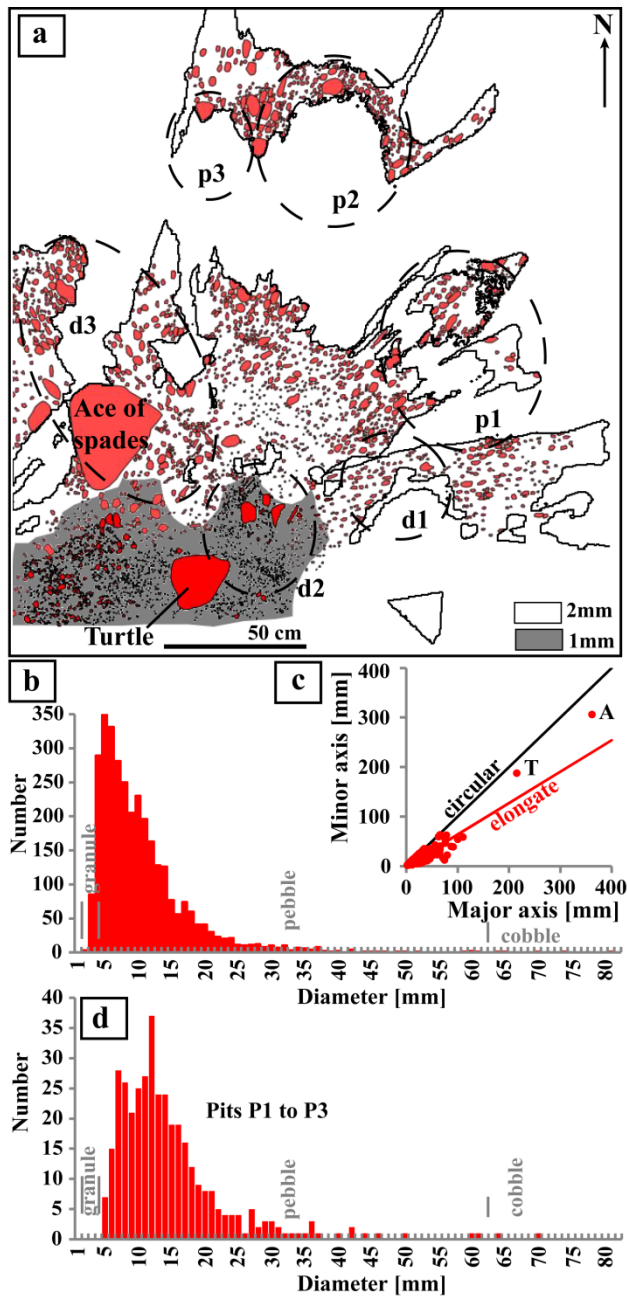


Figure 16. Clast distribution under the lander ($N = 3213$; area = 2.046 m^2). b) Particles sizes over the measured diameter range (range=2 mm to 350 mm; mean=9.08 mm) on which modified Wentworth classes are superimposed (sand, granule and pebble). c) Diagram showing 2D clast shape (equant to sub-equant). A. corresponds to “Ace of Spades” cobble and T to “Turtle” cobble. d) Clast distribution into three pits p1, p2 and p3 ($N = 377$; area = 0.408 m^2).

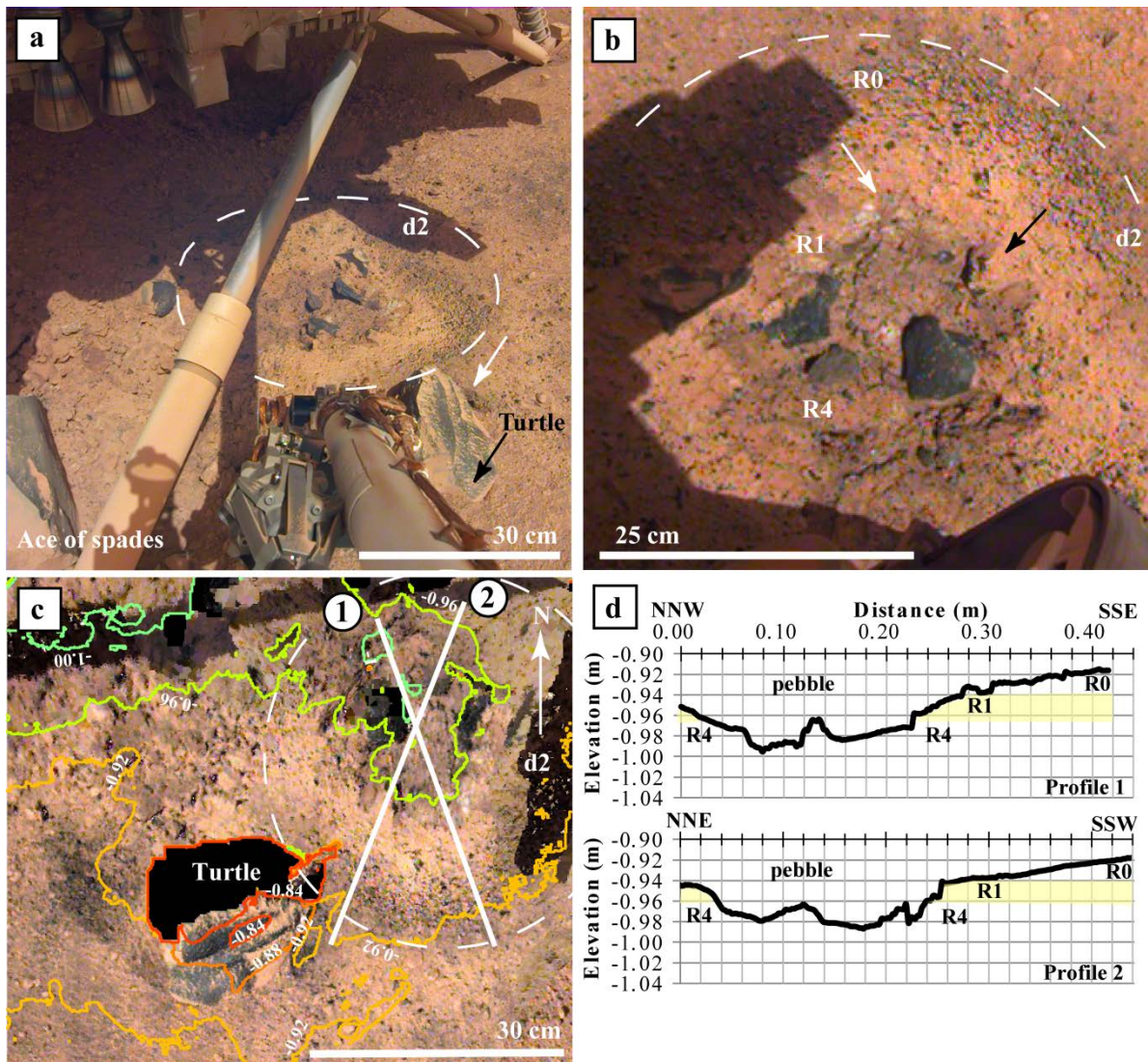


Figure 17: a) IDC image acquired sol 18 under the lander (D002R0018_598131254CPG_F0707_0010M1), showing the shallow depression d1 between the two lander fore feet. Note that the eastern foot (at the upper right corner of image) is sunk into cohesionless, fine, clastic material. The two cobbles (Ace of spades and Turtle) are visible at the front. White arrow indicates small depression behind "Turtle". b) Zoom on the depression d2 (dashed line), viewed by IDC sol 14 (D001L0014_597774194CPG_F0909_0010M1). Three superposed clastic material units are visible: R0, R1 and R4. Notice that the middle unit displays two erosive shapes: small concave scalloped edge with white sides (white arrow) in softer material, and serrated ledge (black arrow) composed of more erosion resistant, tabular, layered material. c) Equi-rectangularly projected IDC image with height contours spaced of 4 cm. White lines correspond to location of topographic profiles. d) Topographic profiles across the depression d2, showing the location of three clastic units viewed in B.

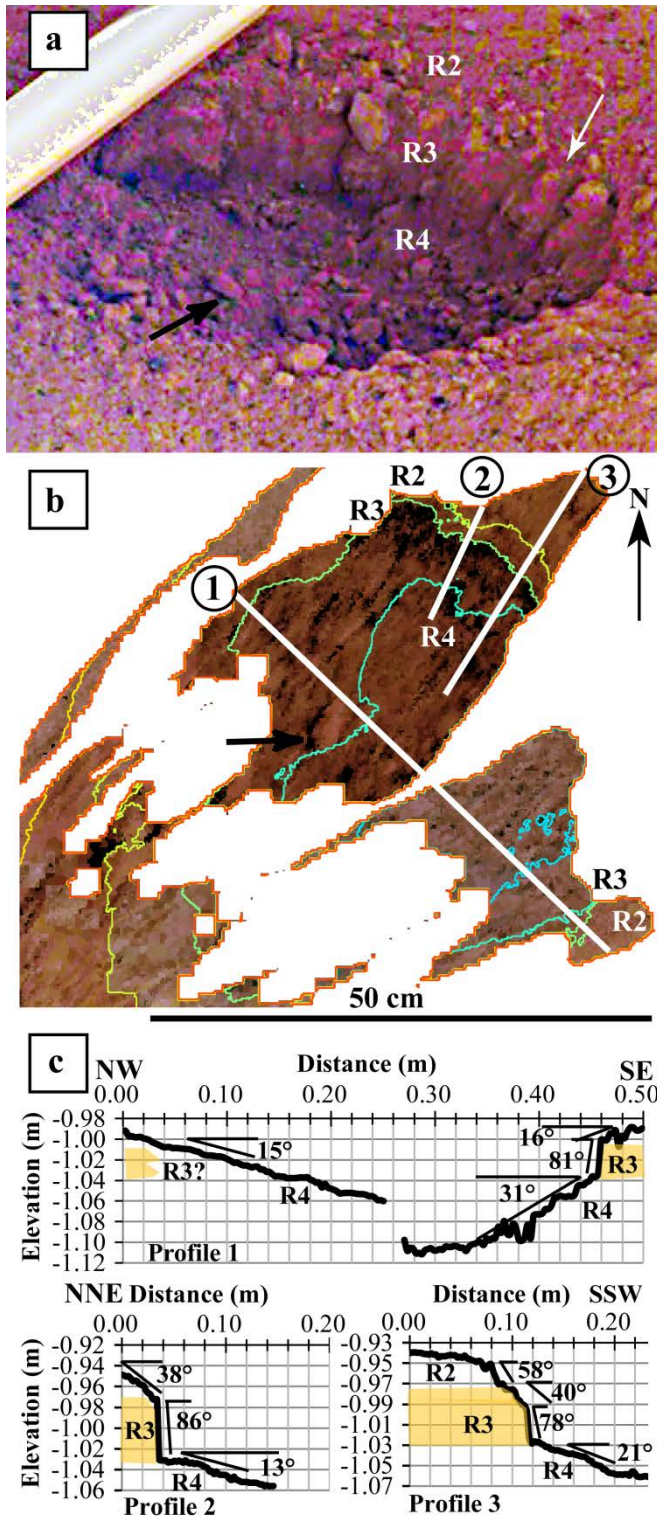


Figure 18. a) Close-up of pit P1 located at the central part under the lander. It is bordered by three superposed clastic units, from top to bottom: R2, sandy to poorly sorted, sub-angular, pebble material; R3, poorly sorted, sub-equant, sub-angular pebbles arranged in a ~5 cm thick, sub-horizontal layer. Some pebbles are longer than wide (white arrow); and R4, cohesionless, poorly sorted, sub-angular gravels. Note that the left side of the pit collapsed (black arrow). b) Mosaic of projected IDC images on which colored lines correspond to elevation contours with an interval of 4 cm. The pit is deep of ~16 cm. The white lines correspond to location of labeled topographic profiles. c) Topographic profiles extracted from DEM on which three units and topographic slopes have been reported. Note that the R3 unit,

composed of pebble material, displays a ~5 cm high, steep slope. The vertical offset viewed in profile 1 is due to low resolution in DEM in this area by a low number of stereo-images.

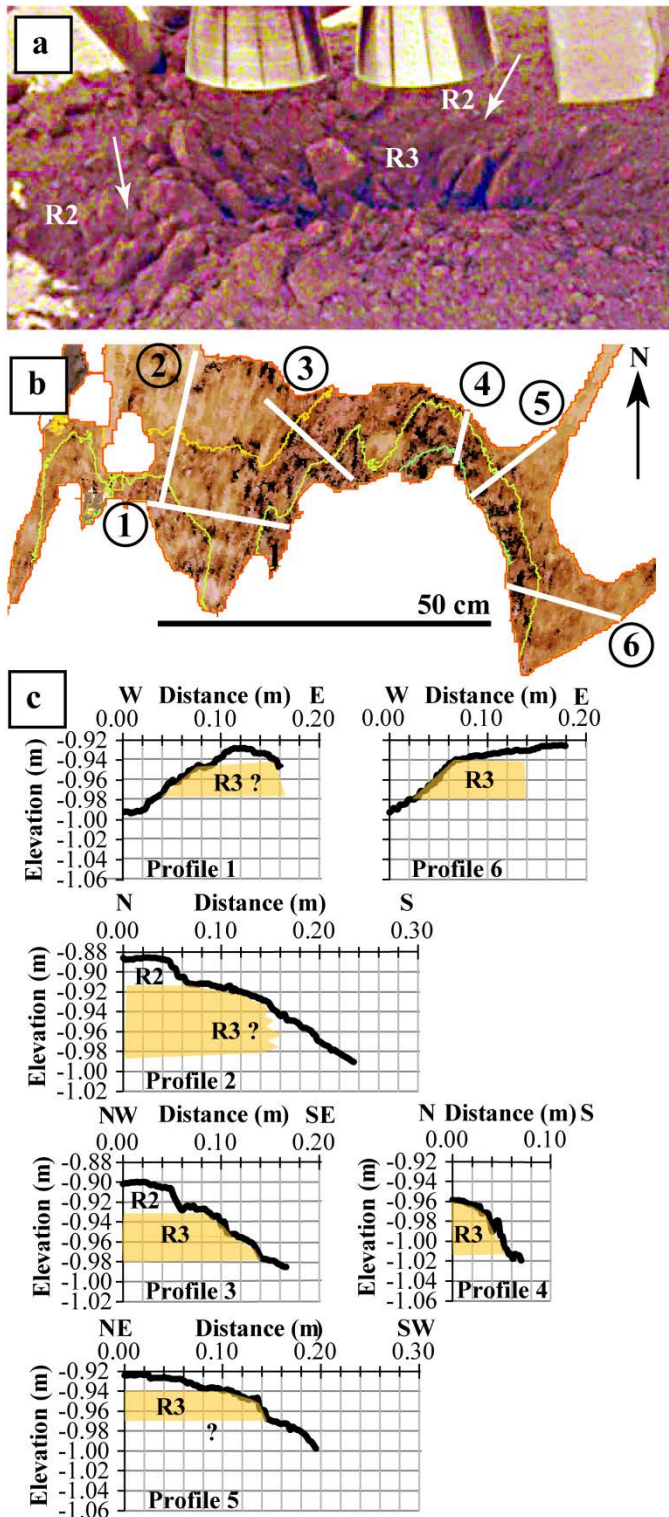


Figure 19. a). Close-up of pits P2 (right) and P3 (left) located at the western side under the lander. They are bordered by two superposed clastic units, from top to bottom: R2, sandy to poorly sorted, sub-angular, gravel material; and R3, poorly sorted, sub-angular pebbles arranged in a ~5 cm thick, sub-horizontal layer. Many pebbles are longer than wide (white arrows), with their longer side arranged sub-vertically and parallel to each other. b) Mosaic of projected IDC images on which colored lines correspond to elevation contours with an

interval of 4 cm. The pit is deep of ~10 cm. The white lines correspond to location of labeled topographic profiles. c). Topographic profiles extracted from DEM on which the R3 unit is labelled. Note that the R2 unit, composed of large pebbles, displays a ~5 cm high, steep slope in the northern side.

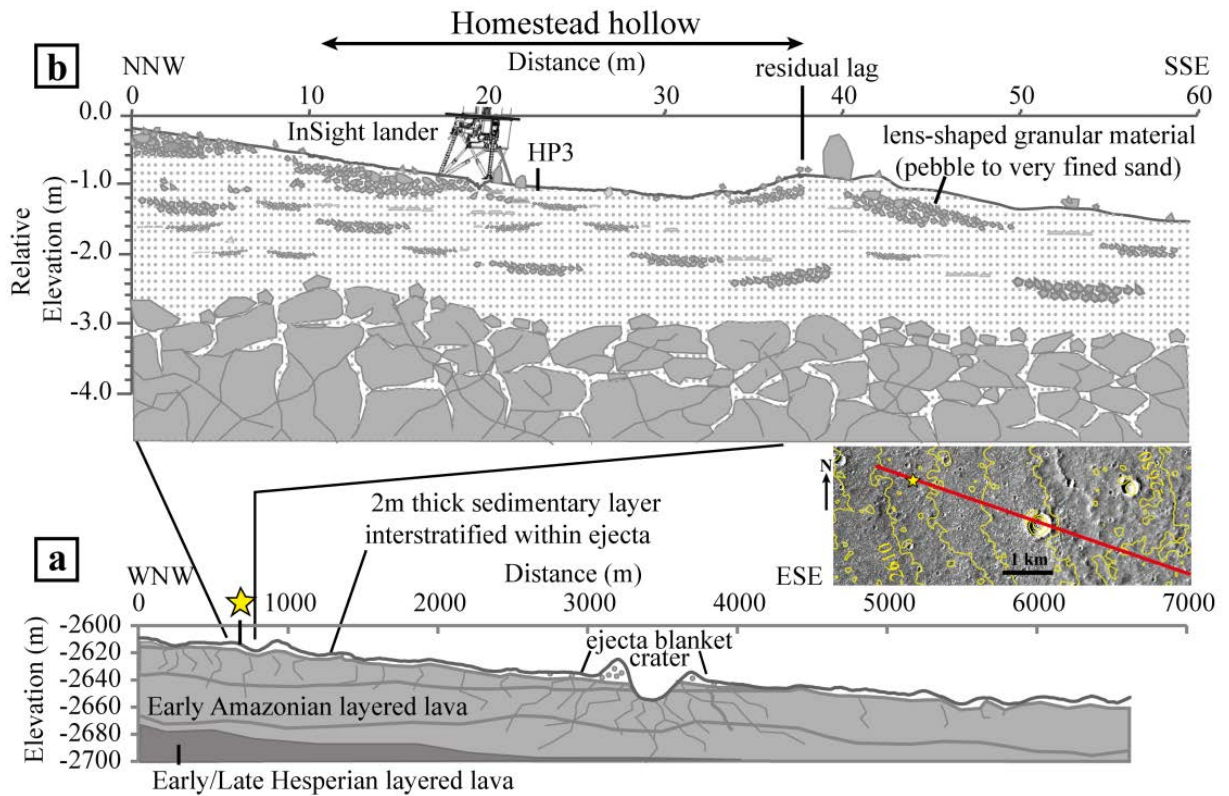


Figure 21: Schematic geologic cross-section across Homestead hollow. a) At CTX scale, the WNW-ESE cross-section shows the superimposition of ~60 m thick, layered lava flows, cratered and fractured by meteoritic impacts, overlapping very thick Early/Late Hesperian volcanic material. A meter thick sedimentary layer covers these lava flows. b) Close-up of the upper layer centered on InSight lander, showing the complex structure of this layer, composed of ejecta blanket and aeolian sediments arranged in fine-fined layered lens-shaped features. Note the vertical axis is exaggerated in this cross-section.